Simulation-based Design of Bioreactors Using Computational Multiphysics

by

Kimia Entezari

A thesis
presented to the University of Waterloo
in fulfillment of the
thesis requirement for the degree of
Master of Applied Science
in
Chemical Engineering

Waterloo, Ontario, Canada, 2021

Author's Declaration

I hereby declare that I am the sole author of this thesis. This is a true copy of the thesis, including any required final revisions, as accepted by my examiners.

I understand that my thesis may be made electronically available to the public.

Abstract

The Covid-19 pandemic highlighted the importance of quickly scaling up the production of vaccines and other pharmaceutical products. These products are typically made within bioreactors: vessels that carry out bioreactions involving microorganisms or biochemical substances derived from microorganisms. The design, construction, and evaluation of bioreactors for large-scale production, however, is costly and time-consuming. Many builds are often needed to resolve issues such as poor mixing and inhomogeneous nutrient transfer. Nevertheless, computational methods can be used to identify and resolve these limitations early-on in the design process. This is why understanding the flow characteristics inside a bioreactor through computational fluid dynamics (CFD) can save time, money, and lives.

Bioreactors contain three phases: 1) a continuous liquid medium which is the host for cells to feed and grow, 2) a dispersed solid phase which is the microorganism particles inside the tank, and 3) a dispersed gas phase which includes the air or oxygen bubbles for microorganisms aspiration. Due to the complexity of solving a three-phase flow problem, most bioreactor multi-phase simulations in the literature neglect the dispersed microorganism phase and its effects entirely–thus assuming two phases only.

In this research project, a hybrid model is developed that captures the effects of all three phases. The model first approximates the liquid and solid phase as a single "mixture" using the drift-flux model. Subsequently, the Euler-Euler method is used to simulate the resulting mixture with the added dispersed gas. This allows the simulation of bioreactors and other bioprocesses with the computational complexity of the two-phase simulation while capturing all three phases.

The "mixture" portion of the model was simulated inside a stirred tank bioreactor. Its results were then validated by comparing them to empirical evidence in the literature. Two parameters were chosen for this validation: 1) the hindered settling velocity of the solid phase in the absence of impeller motion, and 2) the computed power number of the impeller. The validation showed an overestimation of the hindered settling velocity and an underestimation of the impeller power number.

Acknowledgements

Firstly, I would like to thank my supervisor, Professor Abukhdier, for his mentorship, guidance, and support through this project.

I would like to specifically thank James Lowman and Dr. Tanyakarn Treeratanaphitak for their patience answering all my questions, Alex Vasile for reading every sentence of this thesis and helping me to improve it, and Thomas Donnelly for his feedback and friendship during these two years. As well as the COMPHYS group as a whole for the great team environment.

I would also like to thank my dear friends, Elaheh, Mina and Mahshad for all their support, and friendship.

Additionally, I thank Compute Canada for the use of their computational resources.

Lastly, I would like to appreciate my husband, Matin, for all his support, understanding, encouragement, and being my best friend in every moment of this journey. Special thanks to my parents and my brother for their infinite love and support. Thank you Narges joon for all your prayers.

Dedication

To my family.

Table of Contents

List of Figures

List of Tables

Chapter 1

Introduction

1.1 Research motivation

A bioreactor is a controlled system that imitates physiological environments to support a chemical process involving microorganisms [1]. Since microorganisms are susceptible to environmental changes, characterization and fluid flow optimization become essential in bioreactors. However, the design, manufacturing, and evaluation of industrial-sized bioreactors are costly and time-consuming. Thus leveraging the computational methods is an effective way to prevent critical limiting factors, such as insufficient mixing, excessive shear stress, lack of nutrient and oxygen mass transfer, in the early stages of the design process. Computational fluid dynamics (CFD) is used for equipment design and solving fluid flow problems using numerical modeling [2].

Almost all industrial processes operate with multi-phase flows, and bioreactors are not an exception. There are multiple fluid phases within an aerobic bioreactor, see Figure 1.1:

- Gas phase, which is the air bubbles inside the tank for cells' aspiration,
- Liquid phase or media, containing all the nutrition for cells to survive and grow,
- Solid phase, which represents the microorganisms in the system.

CFD simulations of multi-phase flows can provide information that is difficult or infeasible to access via experimentation, such as velocity distribution in the media, oxygen mass transfer between the gas bubbles and the liquid phase, shear stress applied to the cells, cell density in the system *etc.*

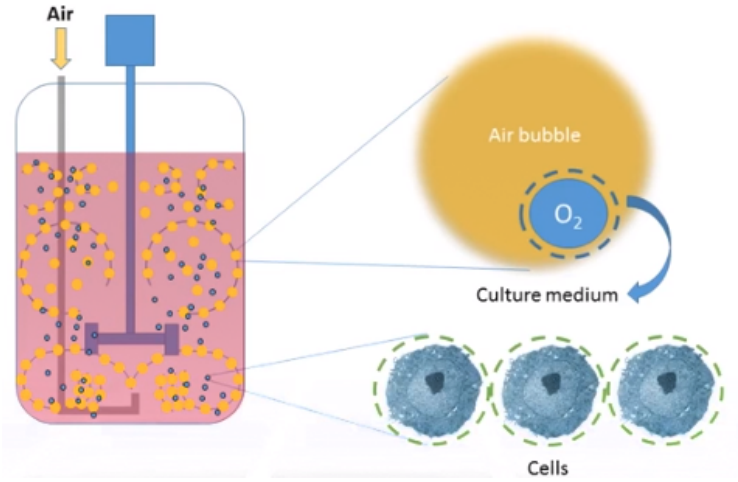

Figure 1.1: Schematic of the three phases present during an aerobic culture inside a stirred tank bioreactor. Yellow circles denote the gas phase, blue circles denote the solid-phase, and the pink domain shows the liquid-phase [3].

There are two main approaches to modeling multi-phase dispersed flows that are feasible for industrial-scale bioreactors: Euler-Euler model (two-fluid model) and Euler-Lagrange model. Depending on the system each approach would have benefits over the other [4]. In the Euler-Euler approach the dispersed phase is treated as a continuum, meaning that it has conservation equations similar to those of the continuous phase [5]. On the other hand, the Euler-Lagrange approach does not consider the dispersed phase as a continuum and solves Newton's equations of motion for each particle [6] with coupling closures for momentum transport between the continuous (continuum representation) and dispersed (particle representation) phases.

Inside an aerobic bioreactor, two dispersed phases are present in the continuous phase (medium): oxygen-containing gas and microorganism cells. There are major differences in the physical characteristics of these two dispersed phases. For example, the physical scale of an average gas bubble (millimeter range [7]) is much larger than the scale of a microorganism (micrometer range [8]). Gas bubbles can have individually different scale and shape, but the size of a microorganism cell stays essentially unchanged during the process. Gas bubbles can burst or coalesce and they have positive buoyancy while microorganisms are neutrally buoyant. With respect to the two main approaches to multi-phase modeling, the Euler-Lagrange model can capture both dispersed phases and even variation between the properties of each dispersed-phase particle. However, it is computationally feasible for relatively small numbers of particles ($10^5 \rightarrow 10^6$ [9]), which is unrealistic for an industrial-

scale bioreactor since they usually contain billions of cells per milliliter of the media. On the other hand, while solving a three-phase problem using the Euler-Euler model, it is still computationally intensive in that transient partial differential equations must be solved, conservation of mass and momentum must be solved for each additional phase, and no steady-state typically exists.

To overcome this problem we are proposing an alternative model that is less computationally intensive and acknowledges all the three phases inside a bioreactor.

1.2 Objectives

This research aims to develop a "hybrid" multi-phase model that enables simulation of industrial-scale bioreactors. For this purpose, an accurate simulation of the hydrodynamics is essential. However, due to the complexity of solving a three-phase flow problem, most of the bioreactor multi-phase simulations in literature neglect the dispersed microorganism phase and its effects entirely [10, 11, 12], assuming only two present phases: the liquid medium and the gas bubbles. Gas-liquid simulations are widely performed in gas-liquid reactors and bubble columns. The presence of dispersed microorganisms (volume fraction more than 1%) has been shown to affect the apparent viscosity of the liquid phase [13] and, consequently, the hydrodynamics observed compared to standard gas-liquid processes. In this research project, a model is developed that captures these effects and transport of the dispersed microorganism phase with significantly reduced computational costs compared to the three-phase Euler-Euler model. This is achieved through approximating the continuous liquid and the dispersed microorganism phase as a single "mixture" using the drift-flux model. This hybrid approach is then used with the two-phase Euler-Euler model for a liquid with dispersed gas, where the liquid is now itself a two-phase "mixture". This allows the simulation of bioreactors and other bioprocesses with the computational complexity of the two-phase simulation, while capturing all three phases. Towards this aim, the objectives are:

- Develop a hybrid three-phase model where the media-biomass is solved as a single "mixture" then this liquid "mixture" with the dispersed air bubbles are solved using the two-fluid model.
- Implement the drift-flux model to treat the liquid and biomass as a single mixture.
- Validate the results against prior published research results.

1.3 Thesis structure

This thesis is organized into seven chapters: Chapter 1 - Introduction, Chapter 2 - Background, Chapter 3 - Literature Review, Chapter 4 - Model Development, Chapter 5 - Validation, Chapter 6 - Stirred Tank Bioreactor Simulation, and Chapter 7 - Conclusions and Future Work.

Chapter 2 explains the background knowledge required to understand this work. In the first section, the change in apparent viscosity as a function of the dispersed phase volume fraction is discussed. In the second section, the relevant multi-phase models to bioreactor simulations are introduced. Additionally, a brief review of the configuration of stirred tank bioreactors is given, and lastly, the scaling parameters for characterizing a bioreactor are described.

Chapter 3 provides an overview of the current literature on the different approaches to simulating biological multi-phase flows in stirred tank bioreactors.

Chapter 4 introduces the development of the hybrid three-phase model. First, the drift-flux model is shown with the derivation of the relative velocity between the phases. Second, the Euler-Euler model is presented along with the momentum transfer terms used in a gas-liquid simulation.

Chapter 5 provides validation for the model using the concept of settling velocity in the absence of impeller movements. The results are compared to an experiment with similar spherical particles.

Chapter 6 shows the simulation set-up and results of the biomass-medium simulations performed using the drift-flux model proposed in Chapter 4. The results for different volume fractions of the microorganisms and different rotational velocities of the impeller were compared.

Finally, Chapter 7 summarizes the conclusions of this work and provides recommendations for future work.

Chapter 2

Background

2.1 Rheology of the Media

The investigation of fluid deformation in relation to the stresses applied is the subject of rheology. Rheology for fluids is commonly characterized by viscosity, and viscosity describes the flow resistance in fluids [14]. Viscosity, μ, is the ratio of the stress, $\boldsymbol{\tau}$, applied to a fluid to the velocity gradient, $\dot{\boldsymbol{\gamma}}$ in that fluid.

$$\mu = \frac{\boldsymbol{\tau}}{\dot{\boldsymbol{\gamma}}} \tag{2.1}$$

Newton's viscosity law is described when the shear stress and shear rate are directly proportional in the above correlation, and the fraction of them is a constant value [15]. Fluids that obey Newton's law of viscosity are called Newtonian fluids. Viscosity in Newtonian fluids is independent of shear strain, and it has a constant value at a given temperature and pressure. On the other hand, when the relation between shear stress and the shear rate has a more complex form, the fluid is said to be non-Newtonian. Eqn. (2.1) is still valid for non-Newtonian fluids, but it is no longer a constant but a function of shear rate, and the viscosity is called the apparent viscosity (μ) [16]. In this section, we briefly talk about Newtonian and non-Newtonian fluids.

2.1.1 Newtonian Fluids

In nature and industry only a small group of fluids exhibit Newtonian behaviour. Gases, water, mineral oils and blends of mineral oils are generally Newtonian in flow behavior [15].

A Newtonian fluid behaviour is shown in Figure 2.1. Based on equation (2.1), viscosity is the slope of shear stress versus shear rate plot. Viscosity in Newtonian fluids (at a specified temperature and pressure) can be determined with one measurement at any shear rate as the plot of viscosity versus shear rate has a slope of zero (viscosity is independent of shear rate).

In multi-phase flows, adding suspended particles to a Newtonian carrier fluid can change the fluid behaviour. Low concentrations of the dispersed phase only change the viscosity value. However, as higher concentrations are added, viscosity is more drastically affected, to a point where the fluid could start behaving non-Newtonian.

2.1.2 Non-Newtonian Fluids

Non-Newtonian fluids can be categorized into three categories based on their reaction to shear rate, see Figure 2.1:

1. Shear-thinning (pseudoplastic), where the viscosity decreases as shear rate increases
2. Shear-thickening (dilatant), where the viscosity increases as the shear rate increases
3. Bingham plastic, where the fluids show a yield stress.

Yield stress is defined as the minimum stress required for a fluid to start flowing. Bingham plastic displays Newtonian behaviour for shear stresses higher than the yield stress. The non-Newtonian behavior of fluids are usually described by already developed empirical models in the literature. Some of the common ones are discussed in this section.

The **power-law** model is widely used due to its capability to describe Newtonian, shear thinning and shear thickening fluid behaviour. According to the power-law model, shear stress is related to shear rate through:

$$\boldsymbol{\tau} = k\ \dot{\boldsymbol{\gamma}}^{n} \tag{2.2}$$

Where k is the flow consistency index (units = Pa s^n) and n is the flow behaviour index (dimensionless). n presents the degree of non-Newtonian behaviour in the fluid. For $n = 1$, the power-law model shows Newton's law of viscosity. For $n < 1$, the model shows shear thinning behaviour and for $n > 1$, shear thickening fluid behaviour is observed [15]. The viscosity in power-law model is:

$$\mu = \frac{\boldsymbol{\tau}}{\dot{\boldsymbol{\gamma}}} = k\ \dot{\boldsymbol{\gamma}}^{n-1} \tag{2.3}$$

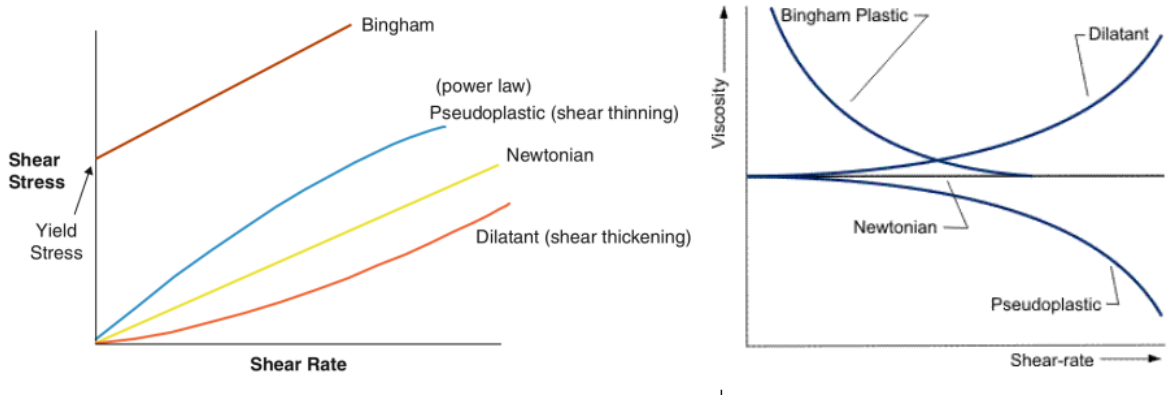

Figure 2.1: Figure on the left shows shear stress vs. shear rate for Newtonian and non-Newtonian fluids [15]. Figure on the right shows viscosity vs. shear rate for both Newtonian and non-Newtonian fluids [17].

The **Herschel-Bulkley** model describes the behaviour of non-Newtonian fluids with yield stress constraint and power-law behaviour for shears greater than yield stress.

$$\begin{cases} \boldsymbol{\tau} = \boldsymbol{\tau}_0 + k\,\dot{\boldsymbol{\gamma}}^n & |\boldsymbol{\tau}| > \boldsymbol{\tau}_0 \\ \dot{\boldsymbol{\gamma}} = 0 & |\boldsymbol{\tau}| < \boldsymbol{\tau}_0 \end{cases} \tag{2.4}$$

Where τ_0 is the yield stress (units = Pa), k and n are the same parameters as in the power-law model. In the case of $n = 1$, the Herschel-Bulkley model describes Bingham plastic fluid behaviour. The viscosity in Herschel-Bulkley model is [17]:

$$\mu = \frac{\boldsymbol{\tau}}{\dot{\boldsymbol{\gamma}}} = \begin{cases} (\boldsymbol{\tau}_0/\dot{\boldsymbol{\gamma}}) + k\,\dot{\boldsymbol{\gamma}}^{n-1} & |\boldsymbol{\tau}| > \boldsymbol{\tau}_0 \\ \infty & |\boldsymbol{\tau}| < \boldsymbol{\tau}_0 \end{cases} \tag{2.5}$$

In multi-phase flows, usually, the addition of suspended particles to a Newtonian fluid reveals shear-thinning behavior [13]. In suspensions, three different regimes can be observed based on the volume fraction of the dispersed phase (α_d) [18]. The upper and lower bounds in each regime can slightly vary depending on the type of the suspended particles:

1. **Dilute regime**, $\alpha_d < 0.01$: In this regime, the apparent viscosity, μ, has a linear relationship with α_d.

$$\mu = \mu_c\,(1 + B\alpha_d) \tag{2.6}$$

μ_c is the viscosity of the pure continuous phase and B is called the 'Einstein coefficient' and takes the value of 2.5.

2. **Semi-dilute regime**, $0.01 < \alpha_d < 0.25$: In this regime, the apparent viscosity shows a higher order dependence on the volume fraction:

$$\mu = \mu_c \left(1 + B\alpha_d + B_1{\alpha_d}^2\right) \tag{2.7}$$

B is the 'Einstein coefficient' and B_1 is derived from the consideration of particle-particle interactions [18]. Lower values of B_1 have been found when Brownian motion and inertia are important [18]. In this regime, the fluid can still be approximated Newtonian.

3. **Concentrated regime**, $0.25 < \alpha_d < \alpha_{max}$: In this regime, the above polynomial correlation no longer holds as the apparent viscosity increases rapidly with α_d, and shows non-Newtonian behaviour. Krieger and Dougherty [19] developed a correlation that successfully predicts the fluid apparent viscosity in the concentrated regime:

$$\mu = \mu_c \left(1 - \frac{\alpha_d}{\alpha_{max}}\right)^{-B'\alpha_{max}} \tag{2.8}$$

Where B' is a fitting parameter. The significance of the above correlation is accounting for the maximum packing fraction, α_{max}, which is the maximum obtained volume fraction of the suspended particles. When α_d reaches the maximum packing fraction, the apparent viscosity tends to infinity and appears as a solid material. The maximum packing fraction depends on the particles' spatial distribution, and therefore it is not a well-defined parameter. However, for uniform spherical particles, it is around 64% [20].

Suspensions in concentrated regime show a yield stress due to the formation of networks between particles. The yield stress is reached when the applied stress is sufficient enough to break up the network. The yield stress has a direct relationship with α_d [21]. Heymann et al. [21] proposed the below relationship for $\boldsymbol{\tau}_0$, where $\boldsymbol{\tau}*$ is a fitting parameter and depends on the size of the particle, see Table 2.1:

$$\boldsymbol{\tau}_0 = \boldsymbol{\tau}^* \left(\left(1 - \frac{\alpha_d}{\alpha_{max}}\right)^{-2} - 1 \right) \tag{2.9}$$

Studies have shown that adding higher concentrations of biomass to a Newtonian fluid can change fluid's apparent viscosity, see Figure 2.2 [13]. In this figure the viscosity goes

Table 2.1: τ^* dependence on particle size [18].

Sphere Radius (μm)	$\boldsymbol{\tau}^*$ (Pa)
1.5	3.12
2.5	0.203
50	4.83 $\times 10^{-2}$

to infinity, 10^3 Pa s, at low shear rates, which shows the presence of yield stress, and the viscosity decreases as shear rate increase, which is a shear-thinning fluid behavior. Therefore, the biological multi-phase shows both shear-thinning and Bingham plastic behavior (Bingham pseudoplastic) at higher concentrations ($\alpha_d > 20\%$) of biomass.

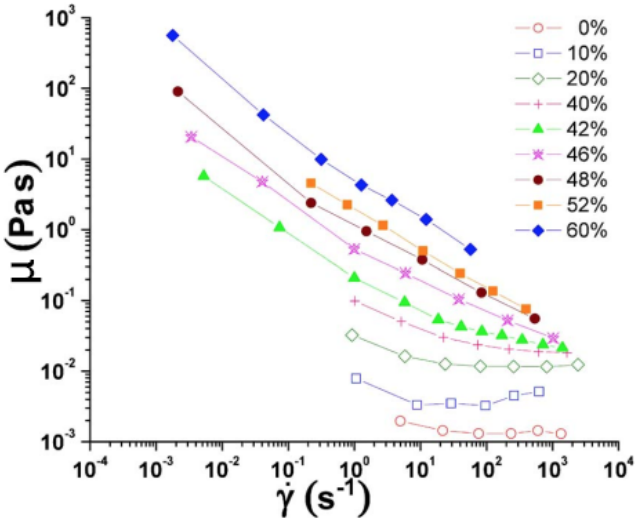

Figure 2.2: Viscosity vs. shear rate at different volume fractions (α_d) of CHO (Chinese Hamster Ovary) cells 0-60% [13].

2.2 Theory and Modeling of Two-Phase Flows

Multi-phase flow is a simultaneous flow with more than one phase and it is found widely in natural environment and industrial processes [22]. Multi-phase flows are usually categorized by the physical states of the accompanying phases and by the topology of the

flow [23]. Due to the complexity of solving multi-phase flows and the extensive amount of effort needed by adding another phase each time, mostly the hydrodynamics of two-phase flows are of interest. There are two main approaches in solving dispersed two-phase flow problems, the Lagrangian approach and the Euler-Euler model, which are discussed in this section.

2.2.1 Lagrangian Approach

In the Lagrangian approach, the dispersed phase particles are tracked through the flow domain, and the momentum equation is solved for each particle. This shows that the particle's motion is related to the sum of forces acting upon it [5].

$$m_p \frac{d\boldsymbol{u}_d}{dt} = \Sigma \boldsymbol{F} \tag{2.10}$$

Where m_p is the particle mass, $\boldsymbol{u}_d$ is the particle velocity and $\Sigma \boldsymbol{F}$ is the summation of individual forces acting on the particle. The right hand side of equation (2.10) can be expanded as [24]:

$$\begin{aligned} m_p \frac{d\boldsymbol{u}_d}{dt} = \frac{m_p}{\tau_p}(\boldsymbol{u}_c - \boldsymbol{u}_d) + m_f \frac{D\boldsymbol{u}_c}{Dt} + \frac{1}{2} m_f (\frac{D\boldsymbol{u}_c}{Dt} - \frac{d\boldsymbol{u}_d}{dt}) + \\ 6{r_p}^2 (\pi \rho_c \mu_c)^{\frac{1}{2}} \int_{\tau_{p0}}^{\tau_p} \frac{\frac{d}{dt}(\boldsymbol{u}_c - \boldsymbol{u}_d)}{(\tau_p - t)^{\frac{1}{2}}} dt + (m_p - m_f) g + \frac{1}{2}(\pi \rho_c {r_p}^2) C_L L V^2 \end{aligned} \tag{2.11}$$

Where τ_p is the particle response time (i.e. the time for momentum transfer due to drag), defined by Eqn. (2.12), $\boldsymbol{u}_c$ is the velocity of the continuous phase, m_f is the mass of fluid displaced by the particle, r_p is the particle's radius, ρ_c is the continuous phase density, μ_c is the dynamic viscosity of the continuous phase, g is the acceleration due to gravity, C_L is the lift coefficient evaluated by Saffman, L the is direction cosines and V is the magnitude of the relative velocity vector.

$$\frac{1}{\tau_p} = (\frac{3}{8 r_p}) C_D \frac{\rho_c}{\rho_d} \|\boldsymbol{u}_c - \boldsymbol{u}_d\| \tag{2.12}$$

The left-hand side of equation (2.11) shows the inertia forces acting on the particle due to its acceleration. On the right-hand side, we have forces due to drag, forces due to the pressure gradient and viscous stresses, the inertia forces of added mass, the Basset forces (the viscous forces due to unsteady relative motion), the buoyancy forces, and the lift forces respectively [24].

In conclusion, by taking the Lagrangian approach to solve a multi-phase problem, Eqn. (2.11) should be solved for a sufficient number of particles in the flow domain. The results are then used to obtain information about the average nature of the flow. However, due to the existence of a significant number of microorganisms inside a bioreactor during an operation, around billions of cells in 1 milliliter of the media, using the Lagrangian approach does not seem feasible as only a limited number of equations can be solved computationally [9]. Therefore, the Lagrangian approach is of limited use in large-scale bioreactor design.

2.2.2 Euler-Euler Model

In the Euler-Euler model both phases, dispersed and continuous, are considered as a continuum. Each phase has its own set of conservation equations and they are coupled together through interphase transfer terms [23]. The conservation of mass (in the absence of interphase mass transfer and reaction) and momentum equations for each phase are (2.13) and (2.14) respectively [23]:

$$\frac{\partial(\alpha_k \rho_k)}{\partial t} + \nabla \cdot (\alpha_k \rho_k \boldsymbol{u}_k) = 0 \tag{2.13}$$

Where α_k is the volume fraction of phase k, ρ_k is the density of phase k and $\boldsymbol{u}_k$ is the mean velocity of phase k.

$$\frac{\partial(\alpha_k \rho_k \boldsymbol{u}_k)}{\partial t} + \nabla \cdot (\alpha_k \rho_k \boldsymbol{u}_k \boldsymbol{u}_k) = -\nabla(\alpha_k P_k) + \nabla \cdot (\alpha_k \boldsymbol{\tau}_k) + \alpha_k \rho_k \boldsymbol{g} + \boldsymbol{M}_k + P_{k,i} \nabla \alpha_k - \alpha_k \cdot \boldsymbol{\tau}_{k,i} \tag{2.14}$$

Where P_k is the phasic pressure, $\boldsymbol{\tau}_k$ is the phasic viscous stress tensor, $\boldsymbol{g}$ is the gravitational acceleration, $\boldsymbol{M}_k$ is the interphase momentum term, $P_{k,i} \nabla \alpha_k$ and $\alpha_k \cdot \boldsymbol{\tau}_{k,i}$ are the contributions of interfacial pressure and shear stress respectively. In the dispersed flow regime these two interfacial forces can be assumed equal in the continuous (c) and dispersed (d) phases ($P_{i,c} \approx P_{i,d} = P_i$ and $\boldsymbol{\tau}_{i,c} \approx \boldsymbol{\tau}_{i,d}$) [25]. The effect of interfacial shear stress is insignificant in the dispersed flow regime therefore it can be neglected [4] and the pressure of the dispersed phase can be approximated by the interfacial pressure, $P_d = P_{d,i}$ [23]. By considering all the above assumptions and approximations the momentum equation for continuous and dispersed phase will be:

$$\frac{\partial(\alpha_c \rho_c \boldsymbol{u}_c)}{\partial t} + \nabla \cdot (\alpha_c \rho_c \boldsymbol{u}_c \boldsymbol{u}_c) = -\alpha_c \nabla P_c + \nabla \cdot (\alpha_c \boldsymbol{\tau}_c) + \alpha_c \rho_c \boldsymbol{g} + \boldsymbol{M}_c + (P_i - P_c) \nabla \alpha_c \tag{2.15}$$

$$\frac{\partial(\alpha_d \rho_d \boldsymbol{u}_d)}{\partial t} + \nabla \cdot (\alpha_d \rho_d \boldsymbol{u}_d \boldsymbol{u}_d) = -\alpha_d \nabla P_i + \nabla \cdot (\alpha_d \boldsymbol{\tau}_d) + \alpha_d \rho_d \boldsymbol{g} + \boldsymbol{M}_d \tag{2.16}$$

The Euler-Euler model can provide a detailed and reliable solution of a two-phase flow field [26]; however, it has some drawbacks including: 1) difficulties in modeling the interfacial momentum transfer terms [26], $\boldsymbol{M}_c$ and $\boldsymbol{M}_c$ terms in Equations (2.15) and (2.16) 2) The interfacial transfer terms can create numerical instabilities and divergence in the solution procedure [27].

2.2.3 Drift-Flux Model

The concept of the drift-flux model is based on considering the mixture as a whole rather than two separate phases. In the drift-flux model, the conservation equations are defined for a single mixture phase. They are derived by adding the two continuity equations and the two momentum equations in the Euler-Euler model. A convection diffusion equation is also derived from the dispersed phase continuity equation to predict the distribution of the dispersed phase within the mixture [23]. Step by step calculation and derivation of the drift-flux model from the Euler-Euler model is provided in Appendix A. In the drift-flux model, the fluid properties are represented by mixture properties making the model formulation simpler than the Euler-Euler formulation [5].

The drift-flux model has three equations, as opposed to the Euler-Euler model, which has four. In the drift-flux model, the interphase momentum transfer terms are eliminated when the two momentum equations are summed, as they are equal in value and opposite in direction. This leads to fewer equations and the elimination of numerical instabilities associated with the interfacial momentum transfer terms. Therefore, the computational resources needed are reduced compared to the two-fluid model.

However, in the drift flux model, some details about the relative motion of the phases are lost due to the mixture assumption, and it needs to be expressed by additional constitutive equations.

By assuming a mixture of only two phases, one continuous and one dispersed, the volume fractions are related through:

$$\alpha_d + \alpha_c = 1 \tag{2.17}$$

Mixture density is calculated through equation (2.18):

$$\rho_m = \alpha_c \rho_c + \alpha_d \rho_d \tag{2.18}$$

We can define the mass-averaged mixture velocity as $\boldsymbol{u}_m$:

$$\boldsymbol{u}_m = \frac{\alpha_c \rho_c \boldsymbol{u}_c + \alpha_d \rho_d \boldsymbol{u}_d}{\rho_m} \tag{2.19}$$

2.2.3.1 Drift-Flux Model Field Equations

The drift-flux model conservation equations are provided here. The full derivation can be found in Appendix A. The mixture continuity equation is:

$$\frac{\partial \rho_m}{\partial t} + \nabla \cdot (\rho_m \boldsymbol{u}_m) = 0 \tag{2.20}$$

The dispersed phase continuity equation in the absence of mass transfer between the phases and reaction is given by:

$$\frac{\partial \alpha_d \rho_d}{\partial t} + \nabla \cdot (\alpha_d \rho_d \boldsymbol{u}_m) = -\nabla \cdot \left(\frac{\alpha_d \rho_c \rho_d}{\rho_m} \, \boldsymbol{u}_{dr} \right) \tag{2.21}$$

And the mixture momentum equation is expressed as:

$$\frac{\partial \rho_m \boldsymbol{u}_m}{\partial t} + \nabla \cdot (\rho_m \boldsymbol{u}_m \boldsymbol{u}_m) = -\nabla \cdot P_m + \nabla \cdot \boldsymbol{\tau}_m - \nabla \cdot \left(\frac{\alpha_d}{\alpha_c} \frac{\rho_c \rho_d}{\rho_m} \boldsymbol{u}_{dr} \, \boldsymbol{u}_{dr} \right) + \rho_m \boldsymbol{g} \tag{2.22}$$

$\boldsymbol{u}_{dr}$ in the mixture momentum equation, Eqn. (2.22), and dispersed phase continuity equation, Eqn. (2.21), is the drift velocity between the phases which accounts for the relative motion between the phases in the drift-flux model and it is defined as:

$$\boldsymbol{u}_{dr} = \alpha_c \boldsymbol{u}_r = \alpha_c (\boldsymbol{u}_d - \boldsymbol{u}_c) \tag{2.23}$$

The second term on the right-hand side of the equation (2.22) is the mixture viscous stress tensor:

$$\boldsymbol{\tau}_m = \Sigma \alpha_k \boldsymbol{\tau}_k \tag{2.24}$$

The drift-flux model formulation has six unknowns, $\boldsymbol{u}_m$ mass-averaged mixture velocity, ρ_m mixture density, P_m mixture pressure, $\boldsymbol{u}_{dr}$ drift velocity, α_c continuous phase volume fraction, and α_d dispersed phase volume fraction. However, the model formulation has three equations and an additional of three constraints are needed to close the model. One of these closures is the phase fraction equality in Eqn. (2.17). The second one is the mixture density equation (2.18) and the last one is a closure for the drift velocity which is derived later in this thesis, see Section 4.1.

2.3 Configuration of Stirred Tank Bioreactors

In this section, the configuration of stirred tank bioreactors (STBs) is discussed. STBs are among the most commonly used pieces of equipment in biochemical processes. They typically contain one or more impellers mounted on a shaft, sometimes baffles, and other internals such as spargers, coils, and draft tubes, shown in Figure 2.3. Numerous parameters including, the type and location of the impellers, the degree of baffling and *etc.* provide control over the performance of stirred tank bioreactors [28]. This section will provide a brief review on the effects of baffles and agitation system on the flow pattern.

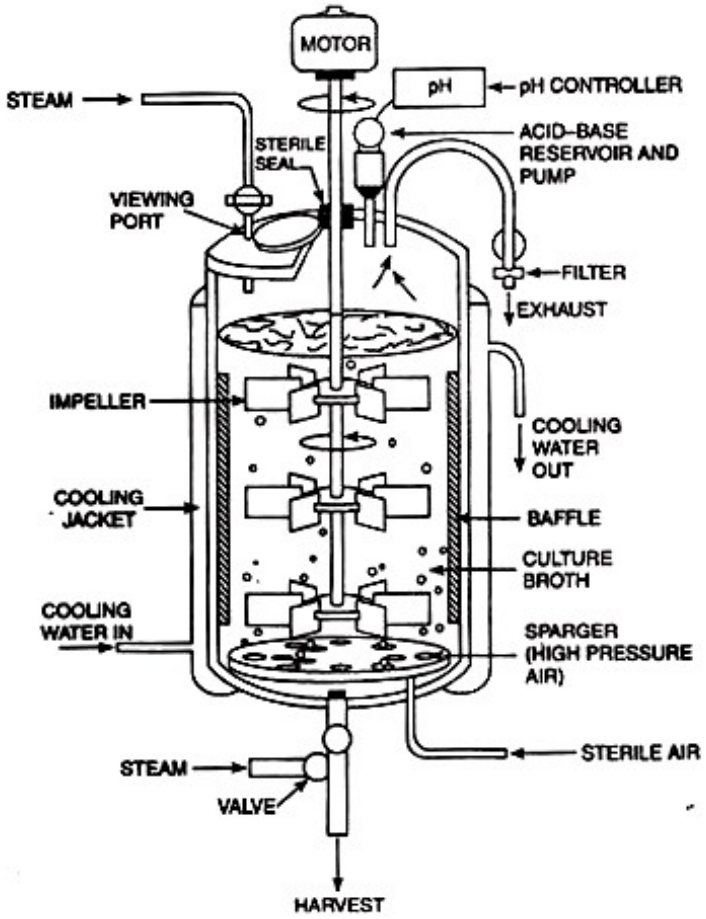

Figure 2.3: Composition of a stirred tank bioreactor [29].

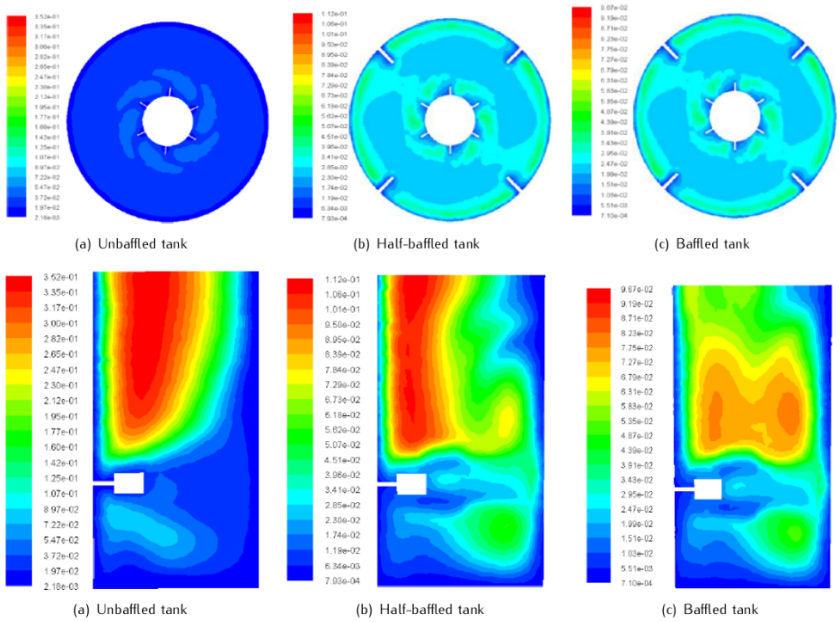

Figure 2.4: First row: Distribution of turbulent viscosity in the $r-\theta$ plane. Second row: Distribution of turbulent viscosity in the $r-z$ plane [30].

Baffles are planes radially-distributed on the interior walls of a vessel. They are typically incorporated into fermentors of all sizes to prevent swirling and vortexing of liquid to improve mixing [31]. Figure 2.4 presents the effect of baffles and their height on the distribution of turbulent viscosity. Turbulent viscosity shows the diffusion mechanism within turbulent flows, and it is enhanced by eddies motions [32]. The fluid homogeneity is improved by turbulent viscosity [30]. In Figure 2.4, from left to right, we have: unbaffled stirred vessel, half-baffled stirred vessel (baffle height = tank height/2), and baffled stirred vessel (baffle height= tank height). Color denotes turbulent viscosity. The first row of the figure ($r-\theta$ cross-section) shows an increase in the turbulent viscosity as the baffles are introduced to the system. The second row ($r-z$ cross-section) shows the effect of baffle length on the turbulent viscosity distribution. The turbulent viscosity is more evenly distributed in the full-length baffle system, and this uniformity decreases as the baffle length is shortened.

An impeller is a rotating internal feature that provides mechanical mixing inside a stirred tank bioreactor to homogenize the distribution of cells, air bubbles, and nutrients. Impellers transmit energy into fluids through flow and shear [34]. Flow is defined as the fluid movement, and shear stress emerges from the fluid velocity gradient. The type

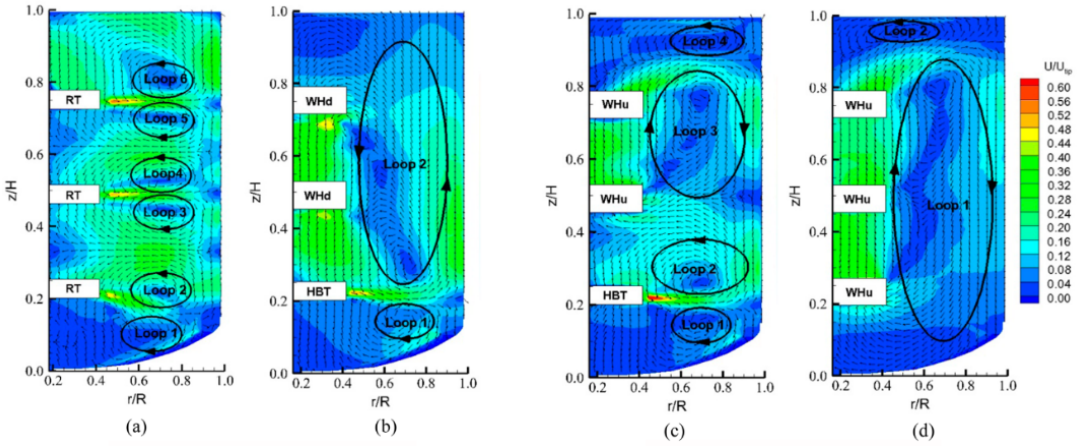

Figure 2.5: Flow fields for different impeller combinations under ungassed condition, RT: Rushton turbine, WHd: Wide-blade hydrofoil impeller pumping down, WHu: Wide-blade hydrofoil impeller pumping up, HBT: Hollow blade turbine [33].

of impeller used has an impact on the flow field. This can be seen in Figure 2.5. In this figure, the velocity distribution is shown for a combination of impeller types. Color denotes fluid velocity over the velocity of the impeller tip (U/U_{tip}); hence blue coded regions show stationary flow. Enhanced fluid movements are observed in case (a) (the majority of the domain is colored green) than in other cases.

2.4 Scaling Parameters

Microorganisms are highly sensitive to their environmental conditions and small changes in them can cause severe damage to the cells and ruining the batch. To avoid this, dimensional analysis is used in order to predict bioreactor performance. Some of these dimensionless groups are:

Power Number

Most of aerobic culture bioreactors in industrial production scale contain one or more impellers. The power consumption of the impellers can be used to directly and indirectly describe mass transfer, heat transfer and mixing in the system [35]. Therefore power number (N_p) is one of the essential dimensionless parameters in

bioreactor design. Power number is the ratio of viscous forces to inertial, and it is obtained from the power input which is related to the impeller torque [36].

$$N_p = \frac{P}{\rho_l {N_i}^3 {D_i}^5} \tag{2.25}$$

$$P = 2\pi N_i \boldsymbol{M} \tag{2.26}$$

where N_i is the impeller rotational speed (RPS), $\boldsymbol{M}$ is the torque acting on the stirrer shaft, and D_i is the impeller diameter.

Impeller Reynolds Number

Impeller Reynolds number, Re_i, is a dimensionless number that helps to predict flow regime within the bioreactor. It describes the ratio of inertial (momentum) to viscous forces. In stirred tank bioreactors, turbulence can be characterized by impeller Reynolds number:

$$Re_i = \frac{\rho_l N_i {D_i}^2}{\mu_l} \tag{2.27}$$

where ρ_l is the liquid phase density, N_i is the impeller rotational speed (RPS), D_i is the impeller diameter and μ_l is the liquid viscosity. In most stirrer tank bioreactors, fluid with Reynolds number greater than 10^4 reaches fully turbulent conditions [37].

Mixing Time

Mixing efficiency is a significant factor impacting the performance of a bioprocess. The mixing efficiency affects the transport processes such as temperature and concentration gradients, as well as pH fluctuations. These changes can substantially damage the microorganisms. Thus, stirring can be used as a determining parameter for the yield of a fermentative process [38]. Mixing time can be used to characterize the quality of stirring in bioreactors. It is defined as the time it takes for a stirring liquid to achieve a specific degree of homogeneity after adding a fixed amount of tracer. The mixing time for a turbulent flow in a stirred tank bioreactor is empirically found to be proportional to [39]:

$$t_m \propto \frac{P}{V^{-\frac{1}{3}}} \tag{2.28}$$

Where P is the power input and V is the liquid volume.

Oxygen Mass Transfer

In most industrial processes, microorganisms grow under aerobic conditions. However, oxygen has low solubility in water-like media, making oxygen mass transfer a critical parameter in bioreactor design. To prevent oxygen depletion in a culture, the oxygen mass transfer rate (OTR) should be equal or greater than the oxygen uptake rate (OUR) by microorganisms. OTR is directly related to the oxygen concentration gradient between the gas-liquid interface and the bulk, and the mass transfer coefficient, k_La, which is affected by the physical properties of the media, type, and concentration of the microorganisms in the system, geometrical aspects of the vessel, etc. [40]. On the other hand, oxygen uptake rate depends on the amount of oxygen entering the vessel, qO_2, and microorganism concentration in the culture, X [41].

$$\underbrace{k_La \cdot (C^*_{O_2} - C_{O_2})}_{\text{OTR}} \geq \underbrace{qO_2 \cdot X}_{\text{OUR}} \tag{2.29}$$

Where $C^*_{O_2}$ is the oxygen concentration at the gas-liquid interface and C_{O_2} is the oxygen concentration in the bulk.

Chapter 3

Literature Review

Aerobic biological cultures are composed of microorganisms dispersed in a multi-phase fluid medium which is water full of soluble nutrients for their survival and growth. In addition to nutrition supply, microorganisms need oxygen to respirate which can be transported to them through an air/liquid free surface or dispersed air bubbles. Thus, biological processes are inherently three-phase. However, due to the complexity of solving a three-phase flow problem and its computational intensity, most of the research done computationally in this area, assume two-phase. Current approaches to modeling two-phase flows are discussed in Section 2.2 of this thesis.

The focus of this literature review is past approaches to modeling multi-phase hydrodynamics in stirred-tank bioreactors. The different approaches taken in literature can be broken down into three categories:

1. The **interface tracking** method where the fluids share an interface with no inter-penetration and the interface is solved to capture the transfer between the phases [10, 42]

2. The **Euler-Lagrange** approach where the fluid is treated as a continuum but the dispersed phase is treated as discrete particles [43, 44].

3. The **Euler-Euler** model where the fluids are approximated as inter-penetrating continua and are solved separately [12, 45, 46].

3.1 Interface Tracking Methods

Another method that is used to simulate multi-phase flows is the interface tracking method. As the name implies, in an interface tracking method, the interface between the phases is captured. This method is well suited for immiscible fluids and segregated flows. However, for large-scale dispersed systems, this approach becomes infeasible due to the study of all of the interfaces between the fluid and the dispersed phase.

The volume of fluid (VOF) is an interface tracking method used in multi-phase systems to track and locate the fluid-fluid interface(s). The VOF model requires the least computational effort compared to the other multi-phase models mentioned above. This is due to 1) no interpenetration between the phases is assumed [36] 2) a single momentum equation needs to be solved as the phases share the same velocity and pressure at the interface [36].

The volume of fluid method is classified as an Eulerian method [47] characterized by a grid that is either stationary or non-stationary. In the case of non-stationary mesh, the mesh moves in a certain way to accommodate the interface evolution. VOF proceeds in two steps [48]:

1. Reconstruction of the interface shape: the interface is approximated using the information on the volume fraction in each cell.

2. Advection of the reconstructed interface in a given velocity field. This results in exchanging the volume of the reference phase across the boundary of neighboring grids.

The volume of fluid method is commonly used in shake flasks, microtiter plates or wave-mixed bioreactors rather than stirred tank bioreactors [36].

Brüning and Botz [10] used the volume of fluid method alongside the continuity and Navier-Stokes equations for incompressible fluids (the process was considered isothermal) to simulate a milliliter-scale stirred tank bioreactor for a gas-liquid system (the effects of microorganisms were neglected). Initially, the gas phase was located in the headspace of the tank, and a free surface was formed where they met. The volume fraction of the liquid was assumed 1 below the free surface and 0 above it. In their work, the interphase mass transfer was analyzed for the performed simulations as the mixing began.

The oxygen mass transfer coefficient, $k_L a$, was calculated in the simulations by deriving the interfacial area, a, from the simulations and determining k_L by [49]:

$$k_L \propto \sqrt{\frac{D_L}{\nu}} \cdot (\epsilon\nu)^{0.25} \tag{3.1}$$

Where $D_L = 2.3 \times 10^{-9}$ m^2/s is a molecular diffusion coefficient of oxygen in water [50]. ϵ is the spatial discretization error determined by Richardson extrapolation [51]:

$$\epsilon \approx \frac{f_1 - f_2}{r^p - 1} \tag{3.2}$$

This method allows using solutions on grids with different refinements to estimate ϵ. f_1 is the solution of the fine grid and f_2 is the coarse grid solution. r is the refinement factor and p is the order of convergence.

The calculated oxygen mass transfer was compared to the experimental results and a constant of proportionality was identified to minimize the deviation. This constant is given in:

$$k_L = 0.167\sqrt{\frac{D_L}{\nu}} \cdot (\epsilon\nu)^{0.25} \tag{3.3}$$

However, the values reported for the constant of proportionality in the literature vary between 0.3 and 0.46 [52, 53].

In Reference [42], the volume of fluid method was used to simulate a 5 L stirred tank bioreactor for stem cell expansion. Stem cells are highly sensitive to shear stress and perform better under slightly hypoxic conditions. Therefore, the purpose of this work was to capture the produced shear stress in the domain for the rotational speed of 60 RPM with no dispersed gas (using the oxygen in the headspace of the tank) to see the system's feasibility for an actual culture. 2.2 L of a 5 L tank was filled with liquid phase (no biomass).

In this work, both the free surface deformation method and the rigid free surface method were simulated to determine whether the simplified approach is acceptable. However, the results showed dependence on the state of the flow (i.e., transient or fully-developed).

To accurately capture the details of the local flow structure to enable precise calculation of produced shear in the domain, the large eddy simulation (LES) method was employed. The Large-eddy simulation is a turbulence method where eddies larger than the filter length are solved via direct numerical simulation (DNS), and eddies smaller than filter length are modeled [54]. When the DNS was not applicable (large eddies), the eddy viscosity (non-zero) was incorporated into the calculation of shear stress:

$$\boldsymbol{\tau} = (\mu + \mu_T)|\overline{\boldsymbol{S}}| \tag{3.4}$$

Where μ is the molecular viscosity, μ_T is the eddy viscosity, and $|\overline{\boldsymbol{S}}|$ is the strain rate given by:

$$|\overline{\boldsymbol{S}}| = \sqrt{2\overline{S_{ij}S_{ij}}} \tag{3.5}$$

In conclusion, the calculated shear stresses were larger than the stem cells tolerance according to literature [55].

3.2 Euler-Lagrange Approach

The Euler-Lagrange approach has the benefit of accurately resolving the motion of an individual droplet/particle in a continuous domain. However, for large-scale simulations and dense populations of the dispersed phase, it can be expensive or computationally infeasible depending on the system.

Lapin [43] applied the Euler-Lagrange approach to characterize a heterogeneous cell population behavior in a stirred tank bioreactor under non-ideal mixing conditions. The main focus of this work was to capture the complex interactions between the extracellular environment and the cell itself. In order to do so, complex and non-linear equations were provided and solved 1) to predict the intracellular state of a single cell along its trajectory and 2) to describe the transport processes across the cell membrane (i.e., substrate uptake rate and product discharge).

100 000 cell particles were simulated inside a 68 L tank using the EL approach. The below equations were proposed for the system, under the assumption that the turbulent flow field is not affected by mass transfer and reactions happening in the system:

$$\frac{d\boldsymbol{x}}{dt} = \boldsymbol{u} \tag{3.6}$$

The above equation shows the convective movement of each cell. The random movement caused by the turbulent dispersion is calculated by:

$$\Delta x_i = \xi_i \sqrt{2 D_T \Delta t} \tag{3.7}$$

Where Δx_i is the random jump in one direction (x, y or z) happening in duration of Δt, D_T is the local eddy diffusivity as a function of turbulent kinetic energy (k) and energy dissipation rate (ϵ), and ξ_i is a random number with the variance value of 1.

Intracellular concentration balance equation is also introduced into the model to predict the intracellular composition of a single cell along its trajectory:

$$\frac{d\boldsymbol{c}_{in,m}}{dt} = \boldsymbol{A}_m \boldsymbol{r}_m(\boldsymbol{c}_{in,m}(t), \boldsymbol{c}_{ex}(\boldsymbol{x}, t)) \tag{3.8}$$

Here, $\boldsymbol{c}_{in,m}$ is the concentration vector of the intracellular compounds inside an individual cell m at time t and $\boldsymbol{c}_{ex}$ is the concentration vector of the extracellular compounds at the

position of the cell $\boldsymbol{x}$ and time t. The $\boldsymbol{c}_{ex}$ is included in the intracellular concentration balance equation to account for the substrate uptake and product discharge transport across the cell membrane. $\boldsymbol{A}_m$ is the stoichiometric matrix of the metabolic reactions in cell m and $\boldsymbol{r}_m$ is the intracellular reaction rates vector which is a non-linear function of $\boldsymbol{c}_{in,m}$ and $\boldsymbol{c}_{ex}$.

The substrate uptake and product discharge transport processes are also included in the Euler simulation of the extracellular state (liquid phase), see Eqn. (3.9). This equation accounts for convection, turbulent diffusion, and the coupling between the extracellular and the intracellular metabolism of the cells:

$$\frac{\partial \boldsymbol{c}_{ex}(\boldsymbol{x})}{\partial t} + (\boldsymbol{u}\nabla)\boldsymbol{c}_{ex}(\boldsymbol{x}) = \nabla \cdot (D_T \nabla \boldsymbol{c}_{ex}(\boldsymbol{x})) + \boldsymbol{S}(\boldsymbol{x}) \tag{3.9}$$

Where $\boldsymbol{S}(\boldsymbol{x})$ is a sink/source term. It is defined as the vector of net transport rates across the membrane of all cells present at position $\boldsymbol{x}$. $\boldsymbol{S}(\boldsymbol{x})$ is obtained by multiplying the sum of all intercellular concentration balance equations by the Dirac delta function, to declare whether cell m is present at $\boldsymbol{x}$ or not:

$$\boldsymbol{S}(\boldsymbol{x}) = V_m \sum_{m=1}^{N_c} \boldsymbol{A}_m \boldsymbol{r}_m(\boldsymbol{c}_{in}(t), \boldsymbol{c}_{ex}(\boldsymbol{x}, t))\ \delta(\boldsymbol{x} - \boldsymbol{x}_m) \tag{3.10}$$

Where N_c is the total number of cells and V_m is the volume of a single simulated cell.

The numerical solution of the problem, Equations (3.6)-(3.9), was challenging due to:

1. Highly non-linear equations, Eqn. (3.8) and $\boldsymbol{S}(\boldsymbol{x})$ in (3.9).
2. The system is stiff because of Eqn. (3.8) and the diffusion term in Eqn. (3.9).
3. The number of equations after discretization is quite large due to the system's three-dimensional nature and consideration of a large number of cells (100 000) to achieve meaningful results.

Lastly, by overcoming all the mentioned obstacles, they simulated a stirred tank bioreactor containing 100 000 yeast cells, results are shown in Figure 3.1. This figure provides snapshots of the combined spatial and temporal dynamics of the intracellular state of the cell population in the bioreactor for a turbulent flow (165 RPM) and a low-turbulence condition (55 RPM). The results demonstrate that the extracellular coupling mechanism acts poorly as the intensity of mixing decreases.

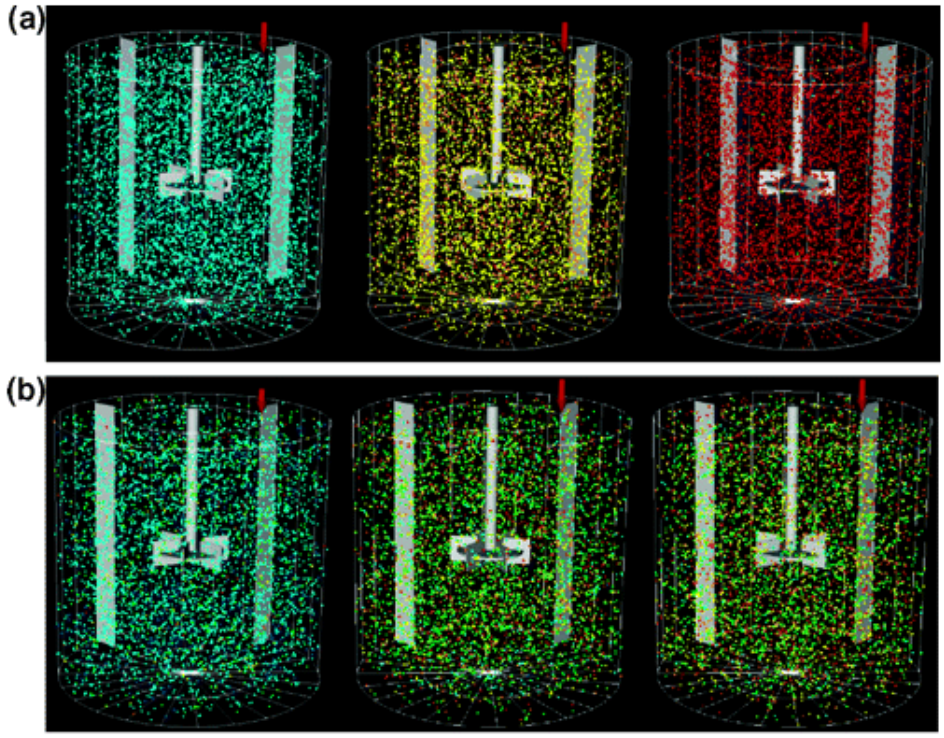

Figure 3.1: Distribution and movement of 100 000 yeast cells inside a three-dimensional stirred tank bioreactor in time. a) $N_i = 165$ RPM b) $N_i = 55$ RPM. The colors indicate the concentration of the intracellular NADH, which increases from magenta (0.1 mM) via cyan, green, and yellow to red (0.22 mM) [43]

3.3 Euler-Euler Model

The Euler-Euler model is an attractive approach for modeling large-scale stirred tank bioreactors. This is because it is the least computationally intensive for the dispersed systems compared to the Euler-Lagrange model and the interface tracking methods mentioned above. In this section, some of the literature on modeling stirred tank bioreactors using the Euler-Euler model are reviewed.

Reference [12] employed the Euler-Euler model to simulate the hydrodynamics and mass transfer inside a 0.18 m^3 stirred tank bioreactor filled with water and dispersed air bubbles. The conservation of mass and momentum were solved for each of the phases (temperature was assumed constant during the operation) and the coupling between the phases

was achieved through pressure and interfacial exchange coefficients. The only considered interphase momentum transfer term was the drag force acting on the bubbles. The drag coefficient was calculated using equation (3.11), where Re_p is the particle/bubble Reynolds number:

$$C_D = \begin{cases} \frac{24(1+0.15{Re_p}^{0.687})}{Re_p}, & Re_p \leqslant 1000 \\ 0.44, & Re_p > 1000 \end{cases} \tag{3.11}$$

$$Re_p = \frac{\rho_L |\boldsymbol{u}_g - \boldsymbol{u}_l| d_b}{\mu_l} \tag{3.12}$$

ρ_l is the water density, $\boldsymbol{u}_g$ is the gas phase velocity, $\boldsymbol{u}_l$ is the liquid velocity, d_b is the average bubble diameter, and μ_l is water viscosity.

Additionally, oxygen mass transfer was evaluated using the k_La parameter. To calculate the k_La values from the CFD simulations, Higbie's penetration theory was employed to estimate k_L. Higbie's model expresses the liquid-side mass transfer coefficient, k_L, in terms of molecular diffusivity of the gas into the liquid phase (D_{AB}) and contact time between the phases (θ), see Eqn. (3.13) [56]. The transfer process is assumed to be under unsteady-state condition. The interfacial area, a, was expressed as a function of the local gas fraction and the local Sauter diameter, d_{32}. Sauter diameter is given by Eqn. (3.14), where d_i is the bubble diameter and n_i is the bubble density [12].

$$k_L = 2\left(\frac{D_{AB}}{\pi\theta}\right)^{0.5} \tag{3.13}$$

$$d_{32} = \frac{\sum_{n=1} n_i d_i^3}{\sum_{n=1} n_i d_i^2} \tag{3.14}$$

In this work, the biomass and its effects were neglected entirely. Two sets of simulations were performed under mammalian cell culture operating conditions for two types of impellers. The simulation results were compared against each other and experimental k_La values, measured from an aqueous medium containing 1.46 g/L K_2HPO_4 and 0.4 g/L KH_2PO_4 to buffer the potential pH changes.

Ding et al. [45] used the gas-liquid Euler-Euler model to evaluate the role of hydrodynamics in the design and optimization of a stirred tank bioreactor (17 L) in biohydrogen production. They assumed a homogeneous mixture of substrate and activated sludge for the liquid phase, where all the components shared the same mean velocity, pressure, and temperature fields. The produced biogas by the fermentation process presented the gas phase in the system. The biogas bubbles were assumed spherical with a mean diameter

of 1 mm. The conservation equations were solved for each phase separately, and the drag force was the only considered momentum transfer term between the phases (drag coefficient formulation was not provided). In this study, the effect of activated sludge was only acknowledged in the physical characteristics of the homogeneous mixture. Two sets of simulations were performed for two types of impellers. The simulation results were compared against each other, and for the sake of validation, the simulated residence time distribution (RTD) was compared to experimental results and showed good agreement.

There is literature on utilizing the Euler-Euler model to simulate micro-carries inside a stirred tank bioreactor. Micro-carriers are support matrices for the growth of adherent cells in bioreactors [46, 57]. They are larger than cells, $100 - 300\mu m$ in diameter, with similar densities. Delafosse et al. [46] analyzed solid-liquid suspension of micro-carriers inside a 1.12 L hemispherical bottom stirred tank bioreactor. They used Cytodex-1 micro-carriers ($d_p = 162\mu m$ and $\rho_p = 1020\text{kg/m}^3$) with a solid concentration of 10% to solve the solid-liquid system. The conservation equations were solved for each phase separately. The drag force was considered as the only momentum exchange term between the phases. Drag force for small volume fractions of the solid phase ($\alpha_s < 0.2$) was modeled using the Wenand-Yu correlation:

$$F_D = \frac{3}{4} C_D \frac{\alpha_s \alpha_l \rho_l |\boldsymbol{u}_s - \boldsymbol{u}_l|}{d_p} {\alpha_l}^{-2.65} (\boldsymbol{u}_s - \boldsymbol{u}_l) \tag{3.15}$$

Where α_s is the volume fraction of the solid phase, α_l is the liquid phase volume fraction, $\boldsymbol{u}_s$ and $\boldsymbol{u}_l$ are the solid phase and liquid phase velocities, respectively. ρ_l is the liquid density and d_p is the diameter of a micro-carrier. C_D is the drag coefficient and it is a function of particle Reynolds number, Re_p:

$$C_D = \frac{24}{\alpha_l Re_p} [1 + 0.15(\alpha_l Re_p)^{0.687}] \tag{3.16}$$

$$Re_p = \frac{\rho_l |\boldsymbol{u}_s - \boldsymbol{u}_l| d_p}{\mu_l} \tag{3.17}$$

To consider the solid particles maximum packing limit ($\alpha_{s,max}$), the granular model was used in the simulations. The granular model considers the maximum packing limit by introducing a solid pressure term ∇P_s into the solid phase momentum equation. The particle-particle interaction force in the solid phase momentum equation was modeled by Syamlal [58].

The simulation results and experiments were compared against each other with respect to solid spatial distribution and just-suspended agitation rate (N_{js}), which is the minimum

impeller speed necessary for all solid particles to maintain off-bottom suspension. The presented modeling approach showed a reasonable estimation of N_{js} and failed to predict the solid spatial distribution inside the vessel accurately. By analyzing the solid spatial distribution results for agitation rates below N_{js}, the volume of the bioreactor can be divided into three regions based on the suspension concentration, shown in Figure 3.2.

1. A clear layer below the free surface at the top of the tank (dark blue region), $\alpha_s \approx 0$.
2. A homogeneous bulk zone (the majority of the tank), $\alpha_s < \alpha_{s,max}$.
3. A packed bed of motionless carriers at the bottom of the tank, $\alpha_s = \alpha_{s,max}$.

The solid concentration in the packed bed region is underestimated for $N < N_{js}$ and is overestimated for $N > N_{js}$.

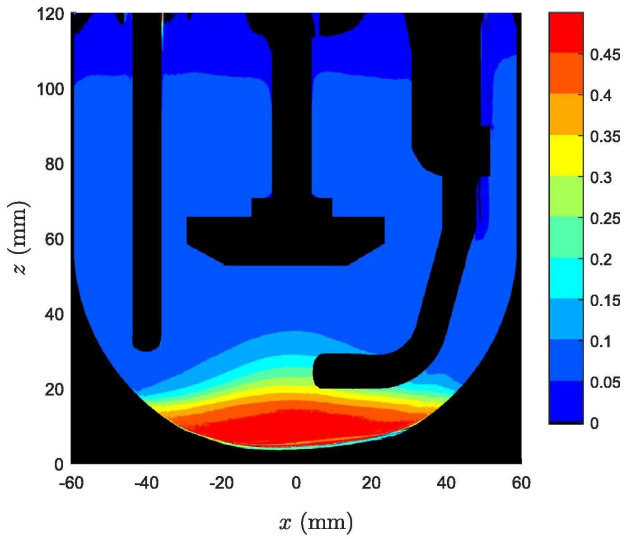

Figure 3.2: Liquid-solid decomposition into three zones for N = 50 rpm. A clear region at the top, a homogeneous bulk in the middle, and a packed bed region at the bottom [46].

In conclusion, the interface tracking methods are not feasible for large-scale simulation of dispersed flows as the resolution of all interfaces between the phases are required [36]. Additionally, for the Euler-Lagrange model to be computationally feasible only a few thousands of cells can be considered which is insignificant compared to the actual number of cells in an industrial process [43]. Lastly, the Euler-Euler gas-liquid simulations

lacked to encounter the effect of the biomass in the system and cannot provide an accurate presentation of a microbiological three-phase flow.

In order to enable a computationally suitable model that encompasses all the three phases, a hybrid three-phase model is developed in this work. This hybrid model approximates the continuous liquid and the dispersed microorganism phase as a single "mixture" using the drift-flux model. Then, the two-phase Euler-Euler model is used to model this liquid phase with the dispersed gas, where the liquid is now itself a two-phase "mixture".

Chapter 4

Model Development

As was mentioned in previous sections, three phases are present inside an aerobic bioreactor:

- A continuous liquid medium which is the host for cells to feed and grow.
- A dispersed solid phase which is the microorganism particles inside the tank.
- A dispersed gas phase which includes the air or oxygen bubbles for microorganisms aspiration.

The inherent character of microorganisms is such that they have similar density to the medium and they are micron-scale small. Consequently, biological multi-phase processes are different from the traditional two-phase and three-phase flows with dispersed gas and solid phases where there is a combination of a large density difference and macroscopic particles. In this chapter, a hybrid multi-phase model is presented which leverages the unique character of the dispersed solid/microorganism phase in biological processes through the combination of two existing multi-phase models: drift-flux (Section 2.2.3) and Euler-Euler (Section 2.2.2). In the presented approach, schematized in Figure 4.1, the continuous liquid phase (medium) and dispersed solid phase (biomass) are treated as a multi-phase "mixture" using the drift-flux model and appropriate closures for the viscous stress [23]. The continuous two-phase mixture is then treated as the continuous phase with a dispersed gas phase using the Euler-Euler model. This approach enables simulation on industrial scales with even less computational complexity than treating all three phases using the Euler-Euler model, without significant loss of accuracy.

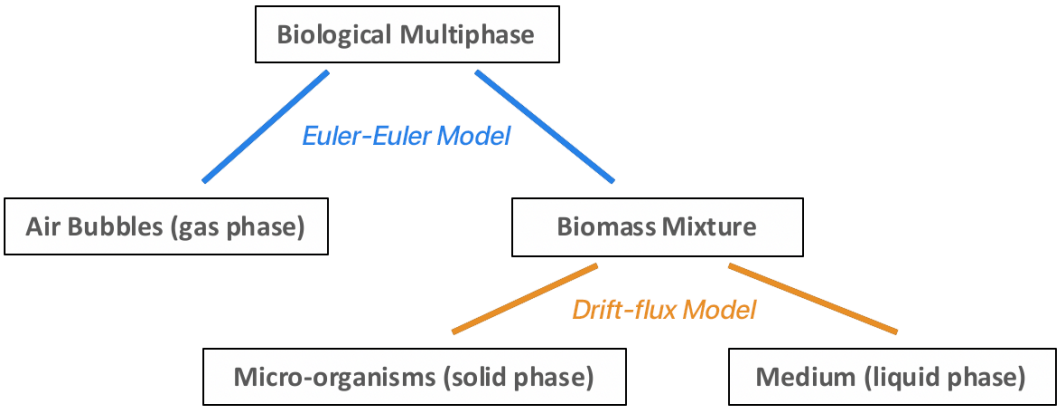

Figure 4.1: Schematic diagram of the multi-phase break down for solving biological three-phase flow

4.1 Continuous Medium and Dispersed Microorganism Using the Drift-Flux Model

The drift-flux model [23] is used to solve the biomass-medium (solid-liquid) composition of the system. As discussed in detail in Section 2.2.3, the basic concept of the drift-flux model is to approximate a multi-phase flow as a single-phase mixture with respect to the conservation of momentum. This requires approximations or closures for both (i) the "drift-flux" of the dispersed phase with respect to the continuous phase and (ii) the viscous stress for the mixture (depending on the velocity and composition). This approach is clearly simpler than the Euler-Euler model, which involves the solution of the conservation of momentum of each of the two phases simultaneously. The drift-flux model is a reasonable approximation for treating the biomass dispersed in medium multi-phase flows due to:

1. the density of the microorganisms is comparable to the carrier fluid - medium density is 1000 kg/m^3, biomass density is 1050 kg/m^3
2. the microorganisms are micron-scale small (40 μm in diameter) which means they have a very high surface area-to-volume ratio, such that drag from the continuous phase is very significant.

For the mentioned reasons the biomass is almost neutrally buoyant, where the buoyancy force shown a for single microorganism is,

$$\boldsymbol{F}_B = m_p \boldsymbol{g} = (\rho_p - \rho_l) V_p \boldsymbol{g} = 1.644 \times 10^{-11} N \tag{4.1}$$

where V_p is volume of a cell and g is the standard gravity $9.81\text{m}^2/\text{s}$. To quantify the competition between the buoyancy force and drag experienced by a single microorganism in a continuous fluid the Stokes number may be used which is a dimensionless value characterizing [59],

$$St = \frac{t_0 u_0}{l_0} \tag{4.2}$$

where (l_0/u_0) is the characteristic fluid flow timescale, l_0 is the characteristic length of the system, u_0 is the fluid velocity, and t_0 is the particle relaxation timescale,

$$t_0 = \frac{\rho_p {d_p}^2}{18 \mu_L} \tag{4.3}$$

For small Stokes numbers ($St \ll 1$), the biomass particles will "follow" the fluid and the buoyancy and drag forces will be balanced, with respect to the hydrodynamic timescale. Conversely, if $St \gg 1$ the microorganism may not always follow the fluid [46]. These two extreme cases are illustrated in Figure 4.2.

In this work, the Stokes number is much less than unity for all the tested conditions (see Section 6.3), meaning the biomass-medium composition can be approximated as a homogeneous mixture.

The drift-flux model is ideal for multi-phase flows where $St \ll 1$. In the following model, the subscript m denotes the "mixture", subscript s denotes the solid phase (biomass), subscript l denotes the liquid phase (medium), and (later) the subscript g denotes the gas phase (air bubbles). For convenience, the defined parameters for the drift-flux model formulation are once again repeated here from Section 2.2.3.

$$\rho_m = \alpha_c \rho_c + \alpha_d \rho_d \tag{4.4}$$

$$\mathbf{u}_m = \frac{\alpha_l \rho_l \mathbf{u}_l + \alpha_s \rho_s \mathbf{u}_s}{\rho_m} \tag{4.5}$$

$$\mathbf{u}_{dr} = \alpha_l \mathbf{u}_r \tag{4.6}$$

$$\boldsymbol{\tau_m} = \Sigma \alpha_k \boldsymbol{\tau}_k \tag{4.7}$$

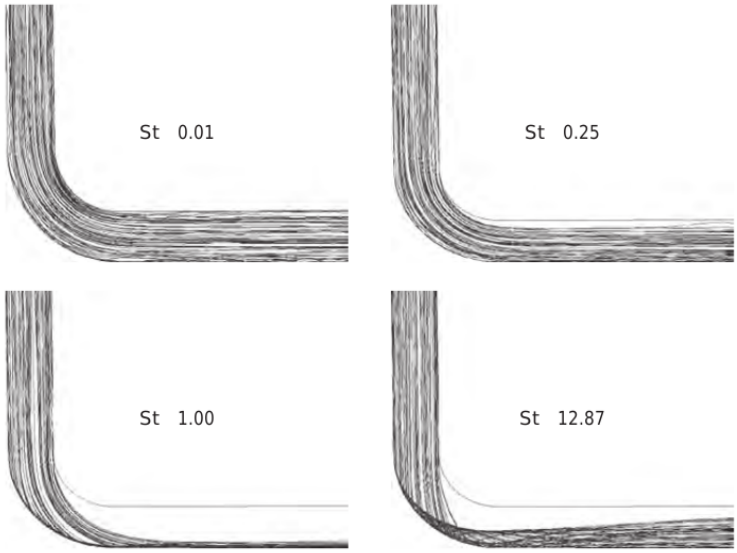

Figure 4.2: Lagrangian particle paths for varying Stokes numbers [59].

For an isothermal two-phase flow the formulation is as follows [23]: Mixture continuity equation is the conservation of mass of the "mixture" which is defined in more detail in Section 2.2.3,

$$\frac{\partial \rho_m}{\partial t} + \nabla \cdot (\rho_m \mathbf{u}_m) = 0 \tag{4.8}$$

Dispersed phase continuity equation is formulated in terms of the mixture velocity and drift flux (closure in closed-form),

$$\frac{\partial \alpha_s \rho_s}{\partial t} + \nabla \cdot (\alpha_s \rho_s \mathbf{u}_m) = -\nabla \cdot (\frac{\alpha_s \rho_s \rho_l}{\rho_m} \mathbf{u}_{dr}) \tag{4.9}$$

Mixture conservation of momentum equation is formulated in terms of the mixture velocity and drift flux (closure in closed-form),

$$\frac{\partial \rho_m \mathbf{u}_m}{\partial t} + \nabla.(\rho_m \mathbf{u}_m \mathbf{u}_m) = -\nabla P_m + \nabla \cdot (\boldsymbol{\tau_m} - \frac{\alpha_s}{\alpha_l} \frac{\rho_s \rho_l}{\rho_m} \mathbf{u}_{dr} \mathbf{u}_{dr}) + \rho_m \mathbf{g} \tag{4.10}$$

The drift-flux model requires an accurate closure for the drift velocity, which captures the relative motion between the phases. By leveraging Newton's second law of motion,

$$\Sigma \mathbf{F} = m\mathbf{a} \tag{4.11}$$

By considering major acting forces on a particle inside the domain, the relative velocity can be derived in closed form for $St \ll 1$. The dominant acting forces on a particle inside a stirred tank bioreactor are, see Figure 4.3:

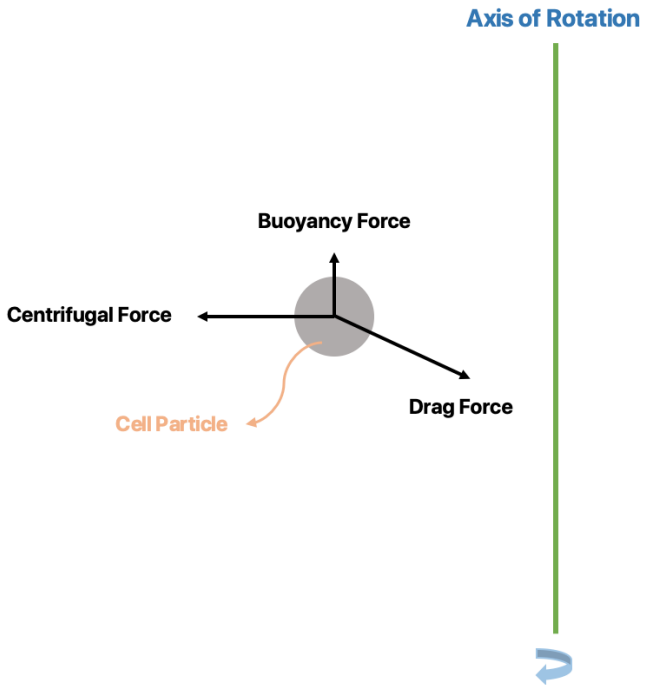

Figure 4.3: Major acting forces on a cell particle inside a stirred tank bioreactor.

Centrifugal force is generated by the agitation system inside the tank. It is an orthogonal force to the axis of rotation that is felt by a particle moving in a curved path. To calculate the centrifugal force, centrifugal acceleration is required. By writing the equations of motion in cylindrical coordinates and making the assumptions of $u_\theta = u_\theta(r)$, $u_r = 0$ and $u_z = 0$ resulting from the centrifugal force, the components in the r-direction simplify to [31]:

$$-\rho_d \frac{{u_\theta}^2}{r} = -\frac{\partial P}{\partial r} \tag{4.12}$$

Where ${u_\theta}^2/r$ is the centrifugal acceleration, a_c. Hence, centrifugal force is:

$$\mathbf{F}_C = m\mathbf{a}_c = (\rho_s - \rho_l)V_p \frac{{u_\theta}^2}{r}\mathbf{e}_r \tag{4.13}$$

where m is the "effective net weight" of a submerged particle in a fluid which is the difference in densities of the particle and its surrounding fluid times the volume of the particle, $(\rho_d - \rho_c)\ V_p$ [16].

Buoyancy force is described by Archimedes' principle, and it is the exerted force on a submerged body. The buoyancy force is equal to the weight of the displaced fluid, and it acts in the opposite direction of gravity vector ($\mathbf{g}_z$).

$$\mathbf{F}_B = (\rho_s - \rho_l)\ V_p\ g\ \mathbf{e}_z \tag{4.14}$$

Drag force is generated when a relative velocity between the two contacting phases exists. The difference in velocity is caused by the imbalance of pressure and shear forces at the interface. Drag acts in the opposite direction of the relative motion of the particle and is given by [60]:

$$\mathbf{F}_D = \frac{C_D}{2}\rho_l A|\mathbf{u}_l - \mathbf{u}_s|(\mathbf{u}_l - \mathbf{u}_s) \tag{4.15}$$

A is the projected cross-section area of the particle perpendicular to the flow direction which is a circle for sphere shaped particles. C_D is the drag coefficient and it is a function of particle Reynolds number, Re_p, see Figure 4.4 [61]:

$$Re_p = \frac{\rho_l|\mathbf{u}_l - \mathbf{u}_s|d_p}{\mu_l} \tag{4.16}$$

d_p is the particle diameter and μ_l is the viscosity of the liquid phase. As can be seen in Figure 4.4, drag coefficient is large at low particle Reynolds numbers and becomes smaller as the Re_p increases. For Re_p greater than 10^3, C_D has a steady value around approximately 0.5 [60].

Including all the mentioned three forces acting on a microorganism, the net force is:

$$\Sigma\mathbf{F} = \mathbf{F}_C + \mathbf{F}_B + \mathbf{F}_D = m_p\ \frac{d\mathbf{u}_s}{dt}$$

and by substituting the above correlations for each force we get:

$$m_p\frac{d\mathbf{u}_s}{dt} = \underbrace{V_p(\rho_s - \rho_l)\frac{u_\theta^2}{\mathbf{r}}}_{\text{centrifugal force}} + \underbrace{V_p(\rho_s - \rho_l)\mathbf{g}}_{\text{buoyancy force}} + \underbrace{\frac{C_D}{2}\rho_l A|\mathbf{u}_l - \mathbf{u}_s|(\mathbf{u}_l - \mathbf{u}_s)}_{\text{drag force}} \tag{4.17}$$

Again, for small Stokes numbers ($St \ll 1$) the dispersed phase is in equilibrium with its surrounding fluid and $\mathbf{u}_s$ does not change much with time:

$$m_p\frac{d\mathbf{u}_s}{dt} \approx 0 \tag{4.18}$$

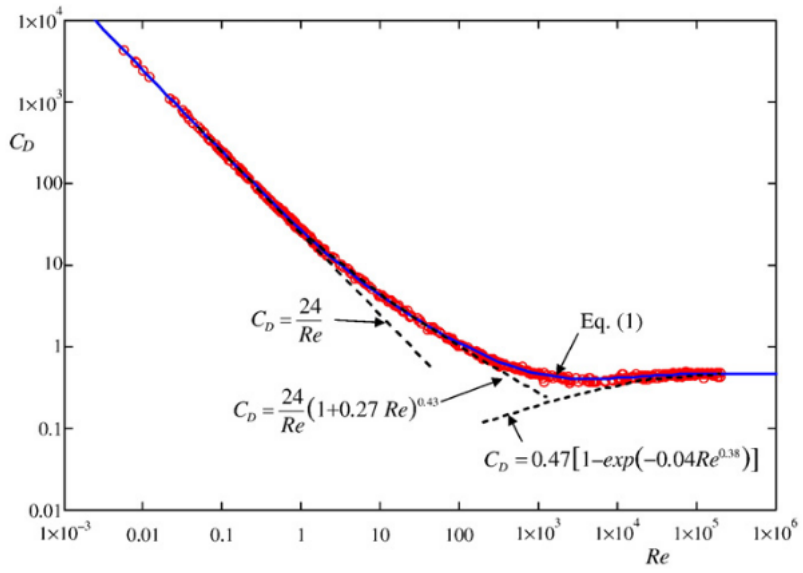

Figure 4.4: Drag coefficient (C_D) vs. particle's Reynolds number (Re) [61].

Therefore Eqn. (4.17) becomes:

$$\frac{C_D}{2}\rho_l A\left|\mathbf{u}_s-\mathbf{u}_l\right|\left(\mathbf{u}_s-\mathbf{u}_l\right)\approx V_p\left(\rho_s-\rho_l\right)\frac{u_\theta^2}{r}\mathbf{e}_r+V_p\left(\rho_s-\rho_l\right)g\mathbf{e}_z \tag{4.19}$$

This means that the drag force is opposing the net force of buoyancy and centrifugal forces, see Figure 4.3. The above equation is in cylindrical coordinate and needs to be converted into Cartesian coordinate for implementation purposes. The following equations are used for the conversion:

$$\mathbf{e}_r=\cos\theta\ \mathbf{e}_x+\sin\theta\ \mathbf{e}_y \tag{4.20}$$

$$u_\theta=\frac{xu_y-yu_x}{\sqrt{x^2+y^2}} \tag{4.21}$$

$$r=\sqrt{x^2+y^2} \tag{4.22}$$

$$\theta=\arctan\left(\frac{y}{x}\right) \tag{4.23}$$

where r, x, and y are the components of position vectors, u_θ, u_x, and u_y are the components of the mass-averaged mixture velocity vectors. By applying the above conversions and assigning $\mathbf{u}_r = \mathbf{u}_s - \mathbf{u}_l$, Eqn. (4.19) becomes:

$$\frac{C_D}{2}\rho_l A\left|\mathbf{u}_r\right|\mathbf{u}_r = V_p\left(\rho_s - \rho_l\right)\left[\left(\frac{xu_y - yu_x}{x^2+y^2}\right)^2 x\mathbf{e}_x + \left(\frac{xu_y - yu_x}{x^2+y^2}\right)^2 y\mathbf{e}_y + g\mathbf{e}_z\right] \tag{4.24}$$

To find the relative velocity from Eqn. (4.24), first the drag coefficient should be acknowledged. As the $St \ll 1$, particles will follow their surrounding fluid and hence the relative velocity has a small magnitude and due to the microscopic nature of microorganisms ($d_p = 40\ \mu$m), particle Reynolds number will be smaller than 1. By looking at Figure 4.4, C_D for $Re_p < 1$ is given by:

$$C_D = \frac{24}{Re_p} \tag{4.25}$$

However, in this work, in order to account for the presence of other particles, the liquid phase viscosity is replaced by the mixture apparent viscosity μ_m in the definition of particle Reynolds number in Eqn. (4.16). The particle Reynolds number used in this work is:

$$Re_p = \frac{\rho_l|\mathbf{u}_l - \mathbf{u}_s|d_p}{\mu_m}$$

Therefore C_D becomes:

$$C_D = \frac{24\ \mu_m}{\rho_l|\mathbf{u}_r|d_p} \tag{4.26}$$

By substituting C_D from the above equation in Eqn. (4.24):

$$12\ \mu_m\frac{A}{d_p}\mathbf{u}_r = V_p\left(\rho_s - \rho_l\right)\left[\left(\frac{xu_y - yu_x}{x^2+y^2}\right)^2 x\mathbf{e}_x + \left(\frac{xu_y - yu_x}{x^2+y^2}\right)^2 y\mathbf{e}_y + g\mathbf{e}_z\right] \tag{4.27}$$

In terms of relative velocity and particle diameter d_p, we have:

$$\mathbf{u}_r = \frac{d_p^2}{18\mu_m}\left(\rho_s - \rho_l\right)\left[\left(\frac{xu_y - yu_x}{x^2+y^2}\right)^2 x\mathbf{e}_x + \left(\frac{xu_y - yu_x}{x^2+y^2}\right)^2 y\mathbf{e}_y + g\mathbf{e}_z\right] \tag{4.28}$$

To summarize, the above correlation for relative velocity varies spatially in the domain and it is derived from all the considered acting forces on a particle inside a stirred tank bioreactor. Since drift velocity is the parameter accounting for the relative motion between

the phases in the drift-flux model, drift velocity as a function of relative velocity is (using Eqn. (4.6)):

$$\mathbf{u}_{dr} = \frac{\alpha_l d_p^2}{18\mu_m}(\rho_s - \rho_l)\left[\left(\frac{xu_y - yu_x}{x^2+y^2}\right)^2 x\mathbf{e}_x + \left(\frac{xu_y - yu_x}{x^2+y^2}\right)^2 y\mathbf{e}_y + g\mathbf{e}_z\right] \tag{4.29}$$

4.2 Inclusion of the Dispersed Gas Phase Using the Euler-Euler Model

Inside a stirred tank bioreactor, the gas phase is dispersed in the biological mixture in the form of distributed air bubbles. The density of the air bubbles ($\approx$ 10 kg/m^3) is considerably smaller than the biological mixture ($\approx$ 1005 kg/m^3). Since the gas phase is very positively buoyant due to the large density difference, it does not follow the carrier fluid path. Therefore, it needs to be treated explicitly, unlike the dispersed microorganism phase, in order to accurately capture its motion. The Euler-Euler model, composed of the continuous medium/dispersed microorganism mixture and dispersed gas, is used to formulate the full three-phase multi-phase model.

The Euler-Euler model is described in Section 2.2.2, where each phase has its own set of conservation equations which are coupled together through interphase transfer terms [23]. The set of conservation equations for each phase are provided here with the assumption of no mass transfer between the phases and no temperature gradient (an isothermal process).

First, for the **mixture phase** the conservation of mass and momentum are (keep in mind that the mixture density, and mixture stress tensor are all phase-averaged),

$$\frac{\partial \rho_m}{\partial t} + \nabla \cdot (\rho_m \mathbf{u}_m) = 0 \tag{4.30}$$

$$\frac{\partial(\rho_m \mathbf{u}_m)}{\partial t} + \nabla \cdot (\rho_m \mathbf{u}_m \mathbf{u}_m) = -\alpha_m \nabla P_m + \nabla \cdot \boldsymbol{\tau}_m + \rho_m \mathbf{g} + \mathbf{M}_m + (P_i - P_m)\nabla \alpha_m \tag{4.31}$$

where $\mathbf{u}_m$ is the mass-averaged mixture velocity from Eqn. (4.5), ρ_m is the mixture density defined in Eqn. (4.4), and α_m is the summation of the volume fraction of the biomass (α_s) and the medium (α_l). The viscous stress tensor of the mixture $\boldsymbol{\tau}_m$ is given by Eqn. (4.7), P_m is the mixture pressure, and P_i is the interfacial pressure between the air bubbles and the medium. It is assumed that each bubble is entirely surrounded by the liquid phase. The interphase momentum transfer term between the mixture and the air bubbles is M_m.

For the **dispersed gas phase** the conservation of mass and momentum take the standard forms,

$$\frac{\partial(\alpha_g \rho_g)}{\partial t} + \nabla.(\alpha_g \rho_g \mathbf{u}_g) = 0 \tag{4.32}$$

$$\frac{\partial(\alpha_g \rho_g \mathbf{u}_g)}{\partial t} + \nabla \cdot (\alpha_g \rho_g \mathbf{u}_g \mathbf{u}_g) = -\alpha_g \nabla P_i + \nabla \cdot (\alpha_g \boldsymbol{\tau}_g) + \alpha_g \rho_g \boldsymbol{g} + \mathbf{M}_g \tag{4.33}$$

where $\mathbf{u}_g$ is the gas phase velocity, ρ_g is the air density, and α_g is the volume fraction of the air bubbles. $\boldsymbol{\tau}_g$ is the gas phase stress tensor, P_i is the interfacial pressure between the air bubbles and the medium, the pressure of the dispersed phase is approximated by the interfacial pressure ($P_g \approx P_i$), and $\mathbf{M}_g$ is the interphase momentum source term.

For the phasic fractions we have:

$$\alpha_m + \alpha_g = \alpha_l + \alpha_s + \alpha_g = 1 \tag{4.34}$$

where α_s is the volume fraction of the solid phase (biomass) and α_l is the volume fraction of the liquid phase (medium).

The interfacial pressure can be calculated by volume averaging the solution of potential flow around a single bubble. The interfacial pressure is,

$$P_i = P_m - C_P \rho_m \mathbf{u}_r \cdot \mathbf{u}_r \tag{4.35}$$

where C_P is the interfacial pressure coefficient. For a uniform distribution of air bubbles, $C_P = 0.25$ [25]. This is approximated by using the inviscid flow solution around the bubble.

The interphase momentum transfer term, $\mathbf{M}$, is the sum of forces from different modes of momentum transfer. In order to close the conservation equations, this momentum transfer term, $\mathbf{M}$, must be defined. The major modes of momentum transfer for a gas-liquid multiphase flow are the drag force, the virtual mass force, the lift force and the wall lubrication force [23].

$$\mathbf{M} = \mathbf{M}_{drag} + \mathbf{M}_{virtual\,mass} + \mathbf{M}_{lift} + \mathbf{M}_{wall} \tag{4.36}$$

Given that the momentum exchange between the phases is equal in value and opposite in direction, the sum of momentum exchange terms between the phases is zero:

$$\mathbf{M}_m + \mathbf{M}_g = 0 \tag{4.37}$$

The **drag force** term is the sum of two forces on a dispersed bubble:

1. Form drag, the effect of non-uniform pressure distribution over a dispersed bubble.

2. Skin drag, the effect of viscous stresses along the bubble surface.

For a dispersed spherical bubble, the drag force formulation for the momentum transfer is given by [23]:

$$\mathbf{M}_{m,drag} = \frac{1}{2}\rho_m \alpha_g \frac{C_D}{r_d}|\boldsymbol{u}_r|\boldsymbol{u}_r \tag{4.38}$$

where C_D is the drag coefficient, r_d is the ratio of the volume to projected area of the bubble, and $\mathbf{u}_r$ is the relative velocity between the mixture phase and the gas phase, $\mathbf{u}_r = \mathbf{u}_m - \mathbf{u}_g$. For a spherical bubble:

$$\mathbf{M}_{m,drag} = \frac{3}{4}\alpha_g \rho_m \frac{C_D}{d_b}|\mathbf{u}_r|\mathbf{u}_r \tag{4.39}$$

Where d_b is the bubble diameter.

The **virtual mass** term in Eqn. (4.36) appears when a bubble moves with a relative velocity in the carrier fluid and it drags a body of the fluid along in its wake. This has the effect of adding extra mass to the bubble, hence the term virtual mass. The added mass is considerable when some acceleration of the bubble occurs relative to the mixture phase, as the added mass also needs to be accelerated [62]. The virtual mass force term is given by:

$$\mathbf{M}_{m,virtual\,mass} = \alpha_g \rho_m C_{VM}\left(\frac{D_g \mathbf{u}_g}{Dt} - \frac{D_m \mathbf{u}_m}{Dt}\right) \tag{4.40}$$

Where C_{VM} is the virtual mass coefficient, $\frac{D_g}{Dt}$ and $\frac{D_m}{Dt}$ are the material derivatives of the gas and the mixture phases, respectively.

The **lift force** in Eqn. (4.36) is a force perpendicular to the main flow direction that is exerted on bubbles and governs the transverse movement of them in the mixture fluid. The lift force is a result of asymmetric pressure distribution and shear forces around the bubbles. The expression for the momentum transfer due to the lift force is [63]:

$$\mathbf{M}_{m,lift} = \alpha_g \rho_m C_L \mathbf{u}_r \times (\nabla \times \mathbf{u}_m) \tag{4.41}$$

where C_L is the lift coefficient.

The **wall lubrication force** in Eqn. (4.36) is a wall effect that appears in gas-liquid bubbly flows. When the liquid phase wets the wall and a bubble rises adjacent to the wall, asymmetric liquid drainage occurs around the bubble. This is due to the no-slip condition on the wall, as the side closer to the wall will drain slower. This asymmetric drainage

forms a hydrodynamic force normal to the wall, which pushes the bubble away from the wall [64]. The wall lubrication force term is represented by [65]:

$$\mathbf{M}_{m,wall} = \alpha_g \rho_m C_W |\mathbf{u}_r - (\mathbf{u}_r \cdot \mathbf{n}_w)\ \mathbf{n}_w|^2 \mathbf{n}_w \tag{4.42}$$

Where C_W is the wall coefficient and $\mathbf{n}_w$ is the unit normal outward on the wall.

Chapter 5

Settling Velocity Validation

5.1 Hindered Settling Velocity Comparison

In this chapter, the mixture portion of the model is validated. The validation was performed using hindered settling velocity in dilute solutions of spherical solid particles. Hindered settling velocity is a phenomenon that states the presence of other particles in a flow reduces the settling velocity of a particle [66]. Unfortunately, no experimental setup is available for a combination of cells and liquid phase without the presence of a gas phase. In aerobic digestion, microorganisms need oxygen for their metabolic reactions and since oxygen solubility in water is poorly, the presence of a gas phase in the system becomes essential. On the other hand, in anaerobic digestion, bacteria produce biogas, e.g. methane, as a byproduct. Therefore, full validation of the model can be arranged after supplementing the system with a gas phase, which is a future work of this project.

5.1.1 Computed Hindered Settling Velocity

The equation of motion on a particle inside the tank is given by Eqn. (4.17). In the absence of impeller rotation, the velocity of a continuous phase will be zero and Eqn. (4.17) becomes:

$$m_p \frac{d\boldsymbol{u}_d}{dt} = V_p(\rho_d - \rho_c)\boldsymbol{g} - \frac{C_D}{2}\rho_c A|\boldsymbol{u}_d|\boldsymbol{u}_d \tag{5.1}$$

At the equilibrium state, the velocity of the dispersed phase is the terminal velocity, which is the measured parameter in experiments. Terminal velocity is the maximum achieved

velocity for a particle falling through a fluid and occurs when the drag force opposes the gravitational force, see Figure 5.1.

$$\frac{C_D}{2}\rho_c A|\boldsymbol{u}_d|\boldsymbol{u}_d = V_p(\rho_d - \rho_c)\boldsymbol{g} \tag{5.2}$$

By substituting C_D from Eqn. (4.26), the terminal velocity becomes:

$$\boldsymbol{u}_d = \frac{d_p^2}{18\mu_m}(\rho_d - \rho_c)\,\boldsymbol{g} \tag{5.3}$$

The above correlation can also be achieved by assigning u_x, u_y, and u_c to zero in Eqn. (4.28) as the fluid is not moving and the velocity components in x and y directions are zero.

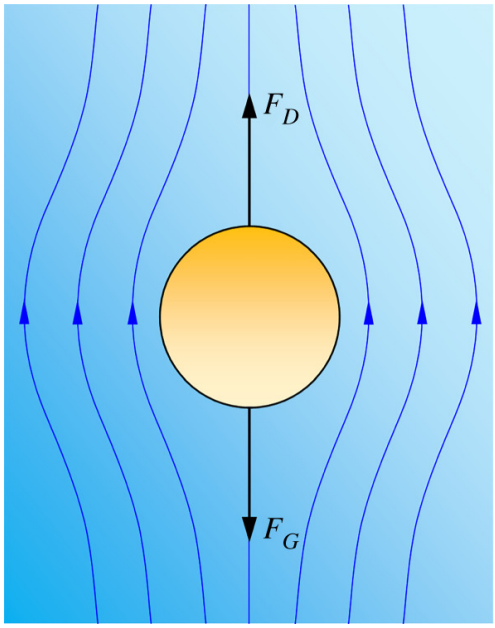

Figure 5.1: Schematic of terminal velocity of a particle. F_D is the drag force and F_G is the gravitational force [67].

In the computed hindered settling velocity, the parameter accounting for the presence of other particles is the apparent viscosity, μ_m. As it was mentioned in Section 2.1, the apparent viscosity is a function of dispersed phase volume fraction, α_d. This relationship

depends on the type and concentration of the particles in a solution. For the tested cases in this work, the apparent viscosity is given by [13]:

$$\mu_m = \mu_c(1 + 2.5\alpha_d + 5.2{\alpha_d}^2) \tag{5.4}$$

Based on the above correlation, apparent viscosity increases by increasing dispersed phase volume fraction as they are directly related. Additionally, increase in apparent viscosity causes the terminal velocity in Eqn. (5.3) to decrease. This behaviour has also been observed in experiments and it is discussed in the next subsection.

5.1.2 Experimental Data of Hindered Settling Velocity in Dilute Solutions

To validate the model, the hindered settling velocity from our model was compared to an experiment with similar particle diameter range and density value. Experiments performed in Ref [68] present the measured mean hindered velocity of monodispersed sphere particles as a function of Pèclet number. Pèclet number characterizes the strength of convection to the strength of diffusion, see Eqn. (5.5). For $Pe \ll 1$, Brownian motion is significant and the particle arrangements are random. For $Pe \gg 1$, the suspension becomes more uniform compared to a random system because convection is dominant. The Pèclet number is given by:

$$Pe = \frac{a\boldsymbol{U}_0}{D_0} \tag{5.5}$$

Where a is the particle's radius, $\boldsymbol{U}_0$ is the Stokes velocity, and D_0 is the Stokes-Einstein diffusion constant for an individual particle:

$$D_0 = \frac{k_B T}{6\pi\mu a} \tag{5.6}$$

Where k_B is the Boltzmann constant , T is the absolute temperature, and μ is the fluid viscosity. By using Stokes velocity formula and Eqn. (5.6) in Eqn. (5.5), the Pèclet number becomes:

$$Pe = \frac{4\pi}{3}\frac{\Delta\rho g a^4}{k_B T} \tag{5.7}$$

In the experiments done by Ref. [68], five different polystyrene particle sizes were suspended in water at 20 ± 0.1 °C. Table 5.1 shows the radius, density, and the Pèclet number of these five samples.

Table 5.1: Experimental parameters in Ref [68]. Radius is in μm and density is in kg/m^3.

Sample	Radius	Density	Pe
PS1	20.94 ± 0.42	1052	9.8×10^4
PS2	10.15 ± 0.2	1052	5.4×10^3
PS3	7.45 ± 0.15	1052	1.6×10^3
PS4	2.55 ± 0.02	1052	2.1×10^1
PS5	1.05 ± 0.02	1052	6.8×10^{-1}

The samples were carried out in 1.5 *ml* or 5 *ml* screw-top vials for volume fractions in the range of 5×10^{-5} to 5×10^{-2} for each particle size. The ratio of the smallest vial dimension to the particle radius was reported to be greater than 350. Therefore, the retarding effect of the container wall is negligible [69]. This ratio is much higher in the simulations done in this project (≈ 3000). The sedimentation velocity of each sample was determined by mapping the settling speed of the particle-supernatant interface using an equipment called cathetometer.

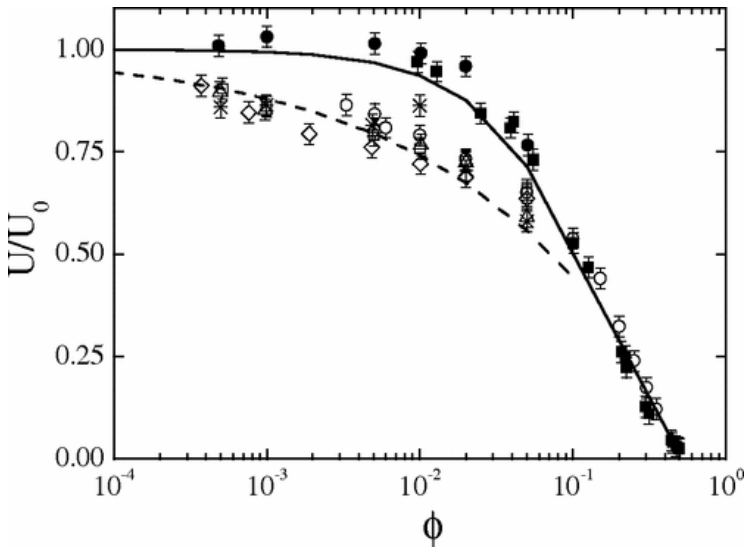

Figure 5.2: Normalized sedimentation velocity U/U_0 vs. volume fraction of spheres Φ. Solid squares are particles with Pe $= 4.8 \times 10^{-2}$, solid circles are particles with Pe $= 6.8 \times 10^{-1}$, stars are particles with Pe $= 2.1 \times 10^1$, open triangles are particles with Pe $= 1.6 \times 10^3$, open diamonds are particles with Pe $= 5.4 \times 10^3$, open squares are particles with Pe $= 9.8 \times 10^4$, and open circles are particles with Pe $= 8.5 \times 10^7$ [68].

Figure 5.2 shows the measured sedimentation velocity, $\boldsymbol{U}$, of all five samples in [68] and two added set of data points from literature (lowest and highest Pe numbers) normalized by the Stokes velocity, $\boldsymbol{U}_0$. The first obvious conclusion is, increase in dispersed phase volume fraction decreases the settling velocity. By further examining the figure, two trends can be seen for the settling velocity behavior as a function of particle's volume fraction. For data with Pèclet number less than 1, the hindered velocity can be approximated by Eqn. (5.8), the solid line in Figure 5.2.

$$\frac{\boldsymbol{U}}{\boldsymbol{U}_0} = (1-\phi)^{6.55} \tag{5.8}$$

Which has the form of Richardson-Zaki [70] correlation (5.9), where n is equal to 6.55.

$$\frac{\boldsymbol{U}}{\boldsymbol{U}_0} = (1-\phi)^{n} \tag{5.9}$$

For data with Pèclet number greater than 1, the hindered velocity can be estimated by Eqn. (5.10) for dilute suspensions, the dashed line in Figure 5.2.

$$\frac{\boldsymbol{U}}{\boldsymbol{U}_0} = 1 - 1.2\phi^{\frac{1}{3}} \tag{5.10}$$

Figure 5.3 shows the comparison between the predicted normalized settling velocity by our model (pink line) and the experimental results produced by Ref. [68] (yellow and orange lines). The green line shows the normalized Stokes velocity. As can be seen in the figure, the numerical model predicts well for low concentrations of the dispersed phase ($\phi < 10^{-3}$) when $Pe < 1$. However, for the considered particles in this work, the Pèclet number is greater than 1 and for $Pe > 1$, there is a significant deviation between the experiments and numerical results.

The presented model in this work only considers the impacts of drag force (one-way coupling) and changes in the apparent viscosity (with volume fraction) for the hindered settling velocity. Therefore, the reasons for this deviation can be due to: 1) underestimation of apparent viscosity by Eqn. (5.4), the settling velocity in Eqn. (5.3) is inversely proportional to apparent viscosity, 2) underestimation of drag coefficient, drag coefficient is also inversely proportional to settling velocity, and 3) not considering the effect of particle motion on the flow (two-way coupling) and particle-particle collisions (four-way coupling) during the settling process [71].

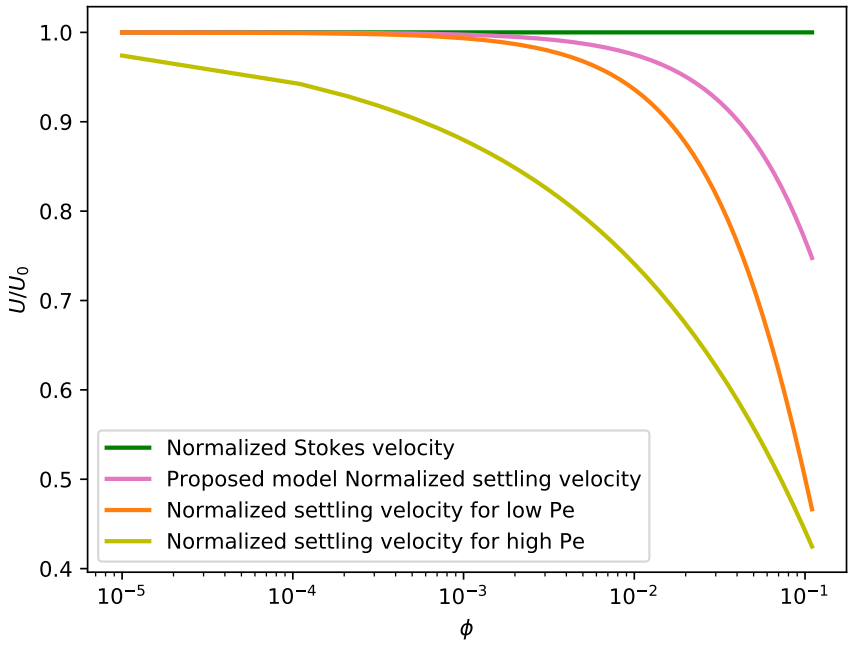

Figure 5.3: Comparison of computed hindered settling velocity and experimental results.

Chapter 6

Stirred Tank Bioreactor Simulation

In this chapter the drift-flux model for medium with dispersed microorganisms (Section 4.1) is used to simulate the hydrodynamics of a stirred tank bioreactor (without gas sparging, for the simulations provided in this chapter $\alpha_s + \alpha_l = 1$). The material properties, operating conditions, and geometry are first described, followed by a brief overview of the numerical methods used to solve the resulting well-posed nonlinear partial differential equation system. Simulation results are then presented for different impeller rotation rates and microorganism loading (reactor volume fraction) and compared to experimental results.

6.1 Geometry and Process Conditions

Stirred tank bioreactors typically follow general guidelines in order to optimize mixing and reduce power consumption [2]. The stirred tank bioreactor used in this project, has a working volume of 1.2 L with a hemispherical bottom and a height to diameter ratio of 1. Additionally, a single impeller is mounted from the top of the tank, along with six baffles attached radially to the interior walls, see Figure 6.1.

The standard design ratios [72] were mostly used to design baffles and the impeller blades, see Figure 6.2. A six-bladed Rushton turbine impeller, which is the most common impeller used in stirred tank bioreactors [33, 73], with a diameter of 5 cm was placed at the center of the tank with a distance of 5 cm from the bottom of the vessel. Six evenly distributed baffles were included, each with a height of 9 cm. The reason behind choosing six baffles was to slightly simplify the meshing process. All the geometrical dimensions of the tank are provided in Table 6.1.

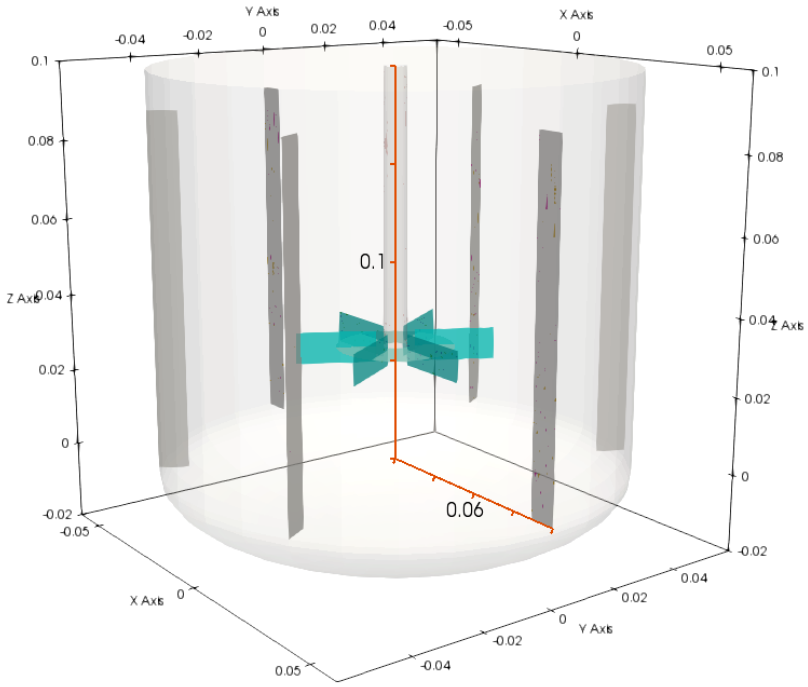

Figure 6.1: Schematic of the modeled stirred tank bioreactor

Table 6.1: Geometrical measurements

equipment	measurement (cm)
Tank height	12
Tank diameter D_t	12
Impeller diameter D_i	5
Baffle height	9
Baffle width W_b	1.2
Blade width W_i	3
Blade length L_i	1

The physical properties used in the simulations are summarized in Table 6.2. An

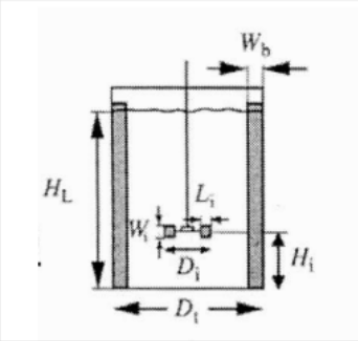

Impeller	D_t/D_i	H_L/D_i	H_i/D_i	Baffles	
				W_b/D_t	Number
1. Rushton turbine $W_i/D_i = 0.2$, $L_i/D_i = 0.25$	3	3	1	0.1	4
2. Paddle $W_i/D_i = 0.25$	3	3	1	0.1	4
3. Marine propeller Pitch = D_i	3	3	1	0.1	4

Figure 6.2: Standard design ratios for bioreactor design [74].

average mammalian cell diameter and density are considered as the biomass (dispersed phase) physical characteristics. The process is assumed isothermal with no mass transfer

Table 6.2: Physical properties

Property	Value
Biomass density (kg/m^3)	1050 [75]
Liquid density (kg/m^3)	1000
Liquid viscosity (Pa.s)	8.9×10^{-4}
Biomass diameter (m)	40×10^{-6}

between the phases and reaction. All the boundaries in the domain are walls with no inlet or outlet (batch process). The initial condition for velocity is that the fluid is at rest; the impeller is assumed to be stationary for $t < 0$. For numerical convenience, the hydrostatic pressure was introduced and solved instead of the static pressure [76]. The hydrostatic pressure is defined as:

$$P' = P - \rho g h \tag{6.1}$$

By using the hydrostatic pressure definition, the mixture momentum equation simplifies to [76]:

$$\rho \left(\frac{\partial \boldsymbol{u}}{\partial t} + \boldsymbol{u} \cdot \nabla \boldsymbol{u} \right) = -\nabla P' + \mu (\nabla \boldsymbol{u}) \tag{6.2}$$

Since there is no flow penetrating the wall, there is no momentum flux through the wall. Solving Eqn. (6.2) in the direction normal to the wall shows that without a momentum

flux, there is no hydrostatic pressure gradient along this normal [77],

$$n_s \cdot \nabla P' = 0 \ Pa/m \tag{6.3}$$

Therefore, the zero-gradient boundary conditions were applied for the hydrostatic pressure. The zero-gradient boundary condition was also applied for the volume fraction of the dispersed phase (α_d) since the momentum flux perpendicular to the wall is zero, Eqn. (6.4). A uniform initial condition was set for α_d (uniform distribution at $t = 0$, homogeneous mixture) along with a maximum packing fraction of 0.65 [13]. The maximum packing fraction was enforced by setting the maximum volume fraction of the dispersed phase to the maximum packing fraction.

$$n_s \cdot \nabla \alpha_d = 0 \tag{6.4}$$

6.2 Biological Flow Simulation Setup

The simulation domain was represented using mostly hexahedron mesh elements generated by the open-source package GMSH [78]. A sample mesh is shown in Figure 6.3, the mesh is complete with boundary layer elements, where the nearest elements to the wall are thinner in the direction normal to the wall. This is due to the no-slip boundary condition. Below the impeller was meshed separately, see Figure 6.4. The mesh was generated with multiple sub-domains, one of which enveloping the impeller with an axially symmetric mesh so that the multiple reference frame (MRF) method could be used for impeller motion.

For mixing to occur in the tank, the impeller needs to rotate. To simulate rotation of the impeller, one must rotate its corresponding mesh. Rotating the mesh is unstable and can be problematic for convergence. By leveraging the Multiple Reference Frame (MRF) method, the mesh movement is substituted by momentum sources in the stationary cells [76]. In the MRF method, the Navier-Stokes equation in the rotating frame can be expressed by the relative velocity [76]. For a general vector, $\boldsymbol{A}$, we have:

$$\left[\frac{d\boldsymbol{A}}{dt}\right]_I = \left[\frac{d\boldsymbol{A}}{dt}\right]_R + \boldsymbol{\Omega} \times \boldsymbol{A} \tag{6.5}$$

Where $\boldsymbol{\Omega}$ is the rotational speed, I denotes inertial, and R denotes rotating frames. For the position vector, $\boldsymbol{r}$, we have:

$$\boldsymbol{u}_I = \boldsymbol{u}_R + \boldsymbol{\Omega} \times \boldsymbol{r} \tag{6.6}$$

Where $\boldsymbol{u}_I$ is the velocity viewed from the inertial frame and $\boldsymbol{u}_R$ is the velocity viewed from the rotating frame. By substituting Eqn. (6.6) in Eqn. (6.2), the Navier-Stokes equation

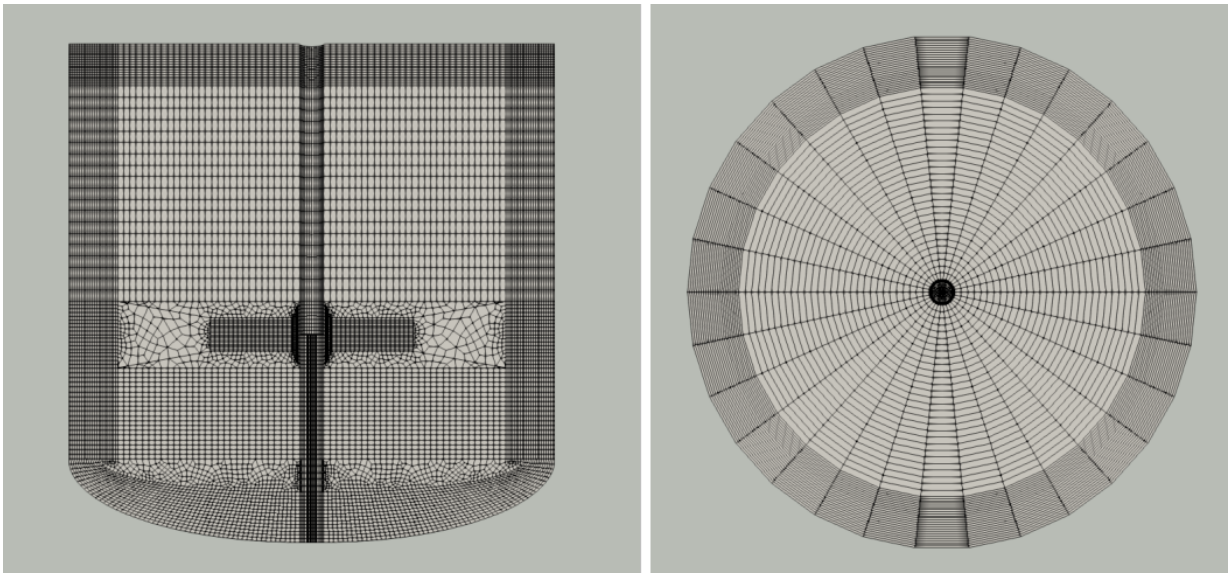

Figure 6.3: Mesh of the geometry visualized with cross-section in XY-plane (left) and the top of the geometry in the XZ-plane (right).

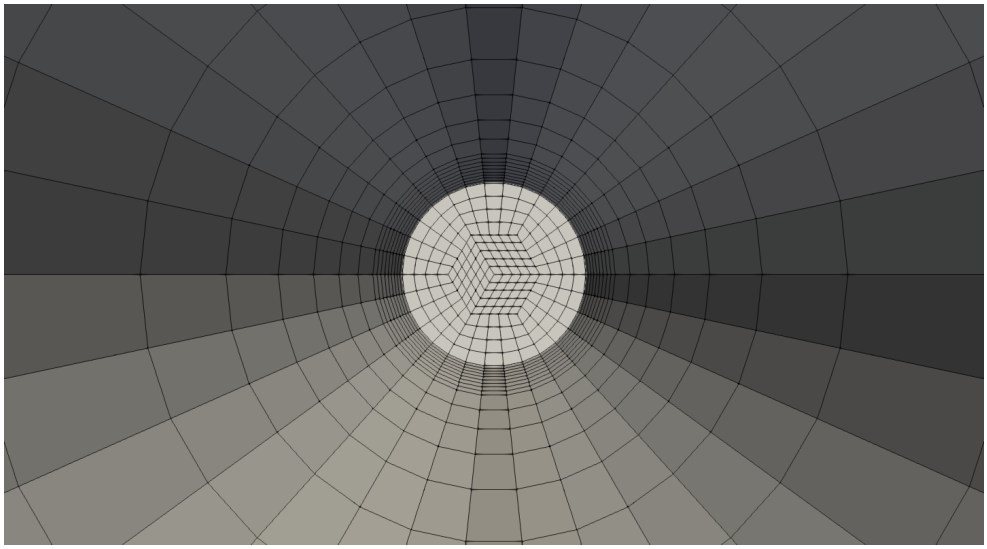

Figure 6.4: Mesh of the center below the impeller.

in the rotating frame becomes,

$$\rho\left(\frac{\partial \boldsymbol{u}_R}{\partial t}+\frac{d\boldsymbol{\Omega}}{dt}\times\boldsymbol{r}+\nabla\cdot(\boldsymbol{u}_R\times\boldsymbol{u}_R)+\underbrace{2\boldsymbol{\Omega}\times\boldsymbol{u}_R}_{\text{Coriolis force}}+\underbrace{\boldsymbol{\Omega}\times\boldsymbol{\Omega}\times\boldsymbol{r}}_{\text{Centrifugal force}}\right)=-\nabla(P')+\mu(\nabla\boldsymbol{u}_R) \tag{6.7}$$

In MRF method, the rotation is assumed to be steady [76]. Therefore, the above equation simplifies to:

$$\nabla\cdot(\boldsymbol{u}_R\times\boldsymbol{u}_R)+\underbrace{2\boldsymbol{\Omega}\times\boldsymbol{u}_R}_{\text{Coriolis force}}+\underbrace{\boldsymbol{\Omega}\times\boldsymbol{\Omega}\times\boldsymbol{r}}_{\text{Centrifugal force}}=-\nabla(P'/\rho)+\nu(\nabla\boldsymbol{u}_R) \tag{6.8}$$

Figure 6.5 shows the performance of using the MRF method as the velocity streamlines are moving in the domain at 90 RPM.

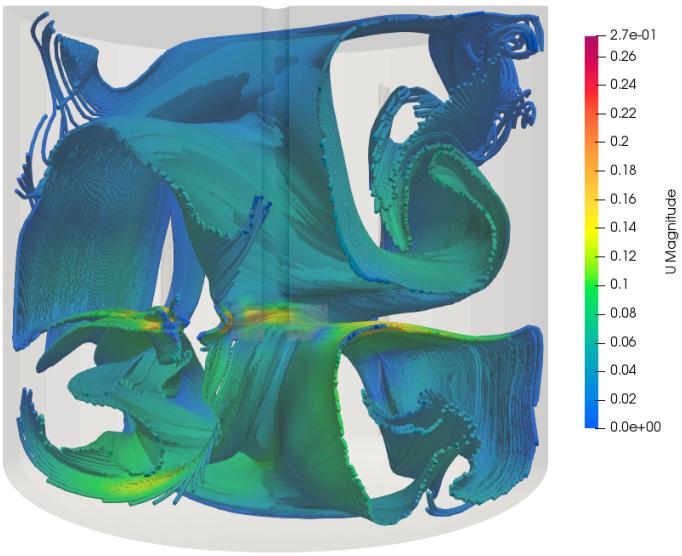

Figure 6.5: Multiple reference frame (MRF) method is used to capture the movement of the impeller without moving the mesh.

All the simulations were performed using an open-source CFD software, built around a finite volume approach, named `OpenFOAM` [79]. The Finite Volume Method (FVM) is a

numerical technique that converts the partial differential equations representing conservation laws into discrete algebraic equations over finite volumes [80]. The first step in the solution process is to discretize the geometry into non-overlapping elements [80]. Then the partial differential equations are discretized into algebraic equations by integrating them over each element and are solved to compute the values of the dependent variables.

The solver used for the simulations is `driftFluxFoam`, which solves a generalized drift-flux model (Equations: (2.20), (2.21), (2.22)) using the merged PISO-SIMPLE (PIMPLE) algorithm [81]. The solver was modified to include both the relevant mixture viscosity model (Section 2.1), [13]:

$$\mu_m = \mu_c(1 + 2.5\alpha_d + 5.2{\alpha_d}^2) \tag{6.9}$$

and the relevant relative velocity/drift-flux model (Section 4.1),

$$\boldsymbol{u}_{dm} = \frac{\rho_c}{\rho_m}(1-\alpha_d)\frac{{d_p}^2(\rho_d - \rho_c)}{18\mu_c}\Big[\big(\frac{xu_y - yu_x}{x^2+y^2}\big)^2 x\boldsymbol{e}_x + \big(\frac{xu_y - yu_x}{x^2+y^2}\big)^2 y\boldsymbol{e}_y + g\boldsymbol{e}_z\Big] \tag{6.10}$$

$\boldsymbol{u}_{dm}$ is called the diffusion velocity and it was used in `OpenFoam` instead of the drift velocity. However, these two quantities are related through:

$$\boldsymbol{u}_{dm} = \frac{\rho_c}{\rho_m}\boldsymbol{u}_{dr} \tag{6.11}$$

The source code for these changes and configuration of the `OpenFOAM` solver are provided in Appendix B . The convergence criteria for residuals were set to 10^{-6} for absolute tolerance and 0.01 for relative tolerance.

6.3 Results and Discussion

Simulations were performed using physical properties in Table 6.2 and auxiliary conditions mentioned in the previous section for three different impeller speeds (30, 60, and 90 RPM) and reactor volume fractions of the dispersed phase (0.01, 0.05, and 0.10) specifying the initial loading of the unit. For all the simulations, the impeller Reynolds number was calculated using the impeller dimensions and mixture apparent viscosity, given in Eqn. (2.27). The Reynolds number varied between 1084.11 and 4110.69, which indicates the transitional and beginning of turbulent flow regimes [31]. Figure 6.6 shows the volume fraction of the dispersed phase, α_d, and the liquid velocity streamlines at various times for 30 RPM impeller speed. The simulation starts with a uniform solution of $\alpha_d = 0.10$, and as expected, at low impeller speeds, as time increases, the microorganisms start to

settle, creating a non-uniform distribution. The blue region at the top of the tank shows minimal values of α_d and gets thicker with time. This represents the migration of biomass towards the bottom due to the dominance of gravitational force over centrifugal force. The red region at the bottom of the tank also expands with time, showing more settled biomass. This behaviour has been witnessed experimentally for similar particles [46] and its observation serves as qualitative experimental validation of the simulation results.

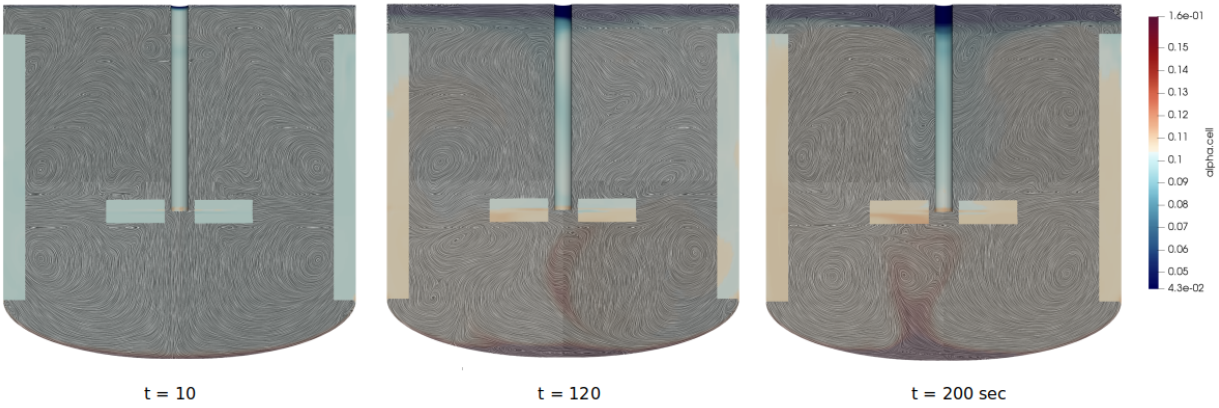

Figure 6.6: Evolution of the phase fraction and liquid velocity streamlines over time. Colors denote α_d. XZ-plane cross-section.

Figure 6.7 shows the cell distribution at 200 second simulation time for three different impeller speeds. By considering the dispersed phase distribution bar on the right-hand side of each bioreactor, one can conclude that increasing rotational speed results in less deviation of α_d from its initial value, in this case, 0.10. This means that the solution stays more homogeneous during the operation for higher RPMs. However, the downsides of increasing rotational speed are excessive produced shear which can harm the microorganisms by breaking them apart [36], and power consumption. Just suspended impeller speed, N_{js}, is the minimum impeller speed that will keep the solid particles off the bottom of the tank. N_{js} is an estimated parameter obtained by dimensional analysis [46]. It has a general form of [82]:

$$N_{js} = S\nu^{\alpha}\left[\frac{g(\rho_s - \rho_l)}{\rho_l}\right]^{\beta} {d_p}^{\gamma} {D_i}^{\delta} X^{\theta} \tag{6.12}$$

Where S is a dimensionless parameter depending on the impeller design and geometric ratios. ν is the mixture kinematic viscosity and X is the solid loading ($M_s/M_{total} \times 100$,

$wt/wt\%$). $\alpha = 0.1$, $\beta = 0.45$, $\gamma = 0.2$, δ = -0.85, and $\theta = 0.12$ (for a Rushton turbine) [82]. In Reference [82], S is defined as:

$$S = a + b\frac{C}{T} \tag{6.13}$$

Where a and b are design parameters, 0.47 and 1.1 (for a Rushton turbine), respectively. C/T is the ratio of impeller location from the bottom (deepest point) to the tank diameter. By substituting the case parameters of this project into Equations (6.12) and (6.13), the just suspended impeller speed, N_{js} for the highest loading ($\alpha_d = 0.10$) is approximately 143 RPM. However, the simulation results for 90 RPM show promising distribution of α_d as the mixture stays almost uniform after 200 second simulation time, see Figure 6.7.

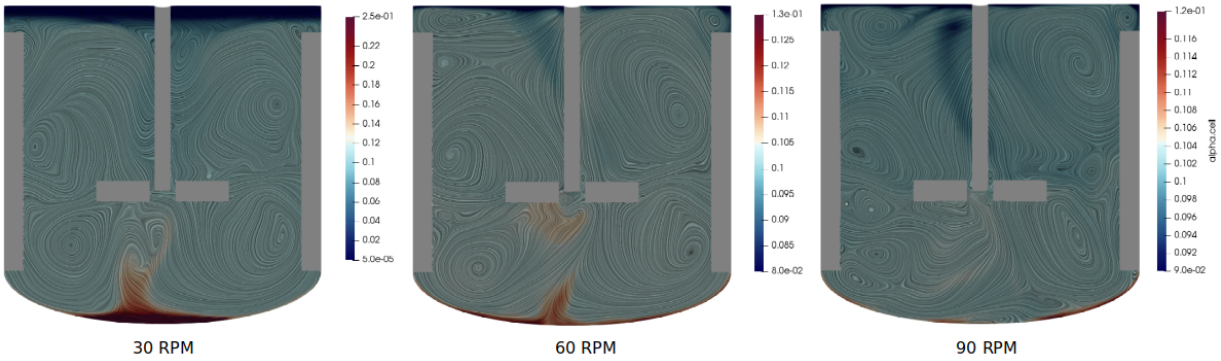

Figure 6.7: Phase fraction and liquid velocity streamlines at 200 sec for different rotational speeds. Colors denote α_d. XZ-plane cross-section.

The mass-averaged mixture velocity, given by Eqn. (2.19), is shown in Figure 6.8 (colors represent the mixture velocity magnitude) for three rotational speeds at 200 sec ($\alpha_d = 0.10$). As expected, increasing the impeller speed results in higher mixture velocity magnitude and a more uniform velocity field. At 30 RPM, the mixture velocity at the top of the tank has zero value, indicating a dead zone with no mixing, and the blue regions near the bottom wall show the motionless settled microorganisms. On the other hand, at 90 RPM, the velocity field looks more uniform and homogeneous than the other two cases. The Stokes number given by Eqn. (4.2) was calculated for all the cases simulated in this work and it was much less than unity for all conditions tested, establishing the idea of particles following the fluid path.

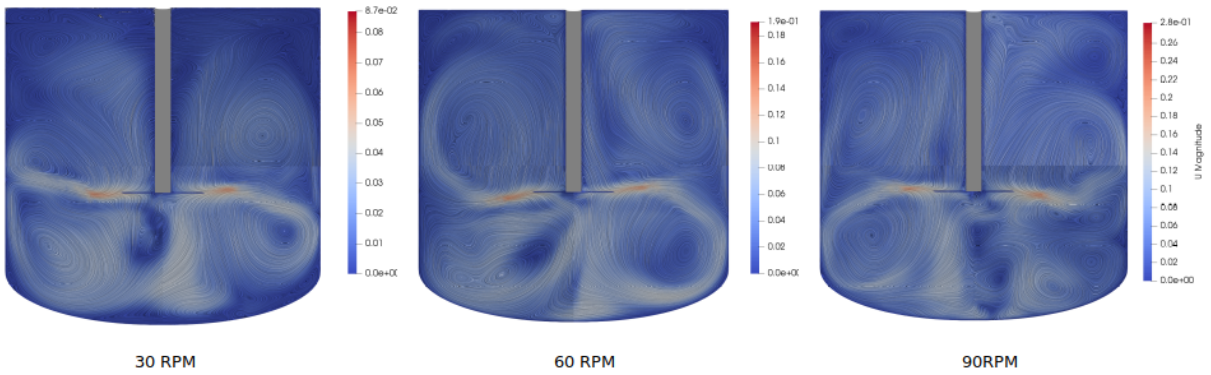

Figure 6.8: Mixture velocity magnitude with velocity streamlines at 200 sec for different rotational speeds ($\alpha_d = 0.10$). YZ-plane cross-section. Color represents the mass-averaged mixture velocity magnitude.

The relative motion between the two phases is quantified by $\boldsymbol{u}_{dm}$, formulated in Eqn. (6.10). Figure 6.9 shows the u_{dm} in x, y, and z directions (colors denote u_{dm} components) for 30 and 90 RPMs with $\alpha_d = 0.10$. As the figure displays, the $u_{dm,x}$ and $u_{dm,y}$ components are zero everywhere except around the impeller where the centrifugal force is most felt by the microorganisms. By comparing the 30 RPM and 90 RPM results, one can conclude that the $u_{dm,x}$ and $u_{dm,y}$ components increase in value as the rotational rate increases. The $u_{dm,z}$ component is independent from rotational speed. This behaviour is expected as the u_{dm} components in x and y directions are dependent on the centrifugal force and $u_{dm,z}$ relies only on the buoyancy force. Therefore, it stays the same for different RPMs.

The buoyancy force is dominant in the tested conditions in this work. This is seen in Figure 6.9, as $u_{dm,z}$ is 10 times greater than the maximum of $u_{dm,x}$ and $u_{dm,y}$ components at 90 RPM, and it is two orders of magnitude higher than the maximum of $u_{dm,x}$ and $u_{dm,y}$ at 30 RPM. Therefore, the magnitude of u_{dm} is highly influenced by $u_{dm,z}$, which is a settling component and it is undesirable for biomass dispersion.

A scaling analysis of Eqn. (4.19) is performed to find the rotational speed at which the centrifugal force becomes the dominant acting force on the particles. The dimensionless quantities are defined as follows: $\tilde{\boldsymbol{v}} = \boldsymbol{v}/v_s$, $\boldsymbol{v}$ represents the relative velocity vector, $\tilde{\boldsymbol{r}} = \boldsymbol{r}/r_s$, $\tilde{\omega} = \omega/\omega_s$, ω is the velocity component in θ-direction. v_s, r_s, and ω_s are the scaling parameters representing characteristic relative velocity, characteristic length, and

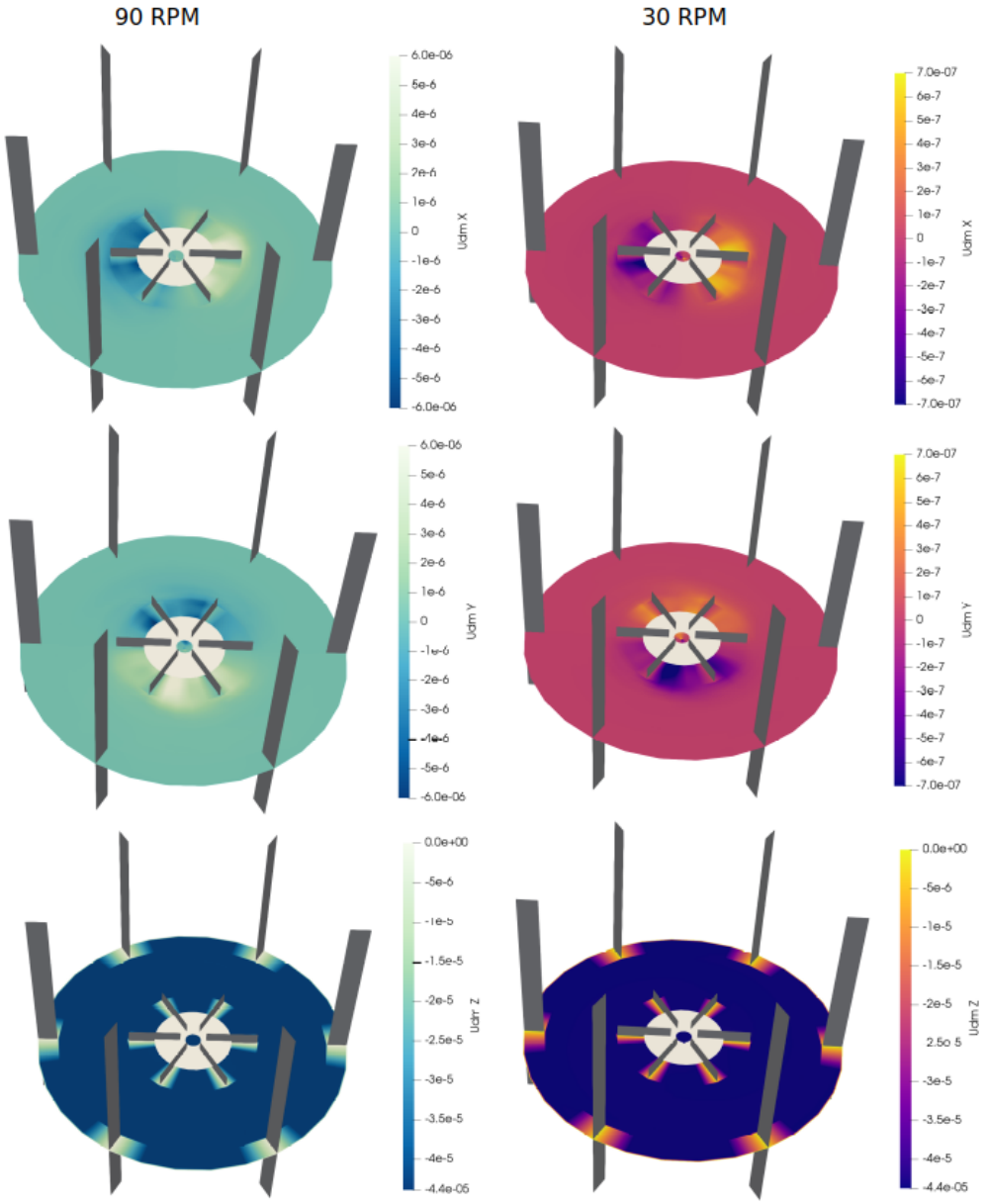

Figure 6.9: XY-plane cross-section for u_{dm} components in 90 and 30 RPMs. The left column shows the results for 90 RPM and the right column shows the results for 30 RPM. Colors represent u_{dm} components.

characteristic angular velocity. This results in the following equation:

$$\frac{C_D}{2}\rho_l A {v_s}^2 \left|\tilde{\boldsymbol{v}}\right| \tilde{\boldsymbol{v}} = V_p \left(\rho_s - \rho_l\right) \frac{{\omega_s}^2}{r_s} \frac{\tilde{\omega}^2}{\tilde{\boldsymbol{r}}} \mathbf{e}_r + V_p \left(\rho_s - \rho_l\right) g \mathbf{e}_z \tag{6.14}$$

Dividing the equation by $\frac{C_D}{2}\rho_l A {v_s}^2$ results in:

$$\left|\tilde{\boldsymbol{v}}\right| \tilde{\boldsymbol{v}} = \frac{2V_p \left(\rho_s - \rho_l\right)}{C_D \rho_l A {v_s}^2} \frac{{\omega_s}^2}{r_s} \frac{\tilde{\omega}^2}{\tilde{\boldsymbol{r}}} \mathbf{e}_r + \frac{2V_p \left(\rho_s - \rho_l\right) g}{C_D \rho_l A {v_s}^2} \mathbf{e}_z \tag{6.15}$$

Now for the centrifugal force to be dominant, the scaling parameter in the centrifugal term must be greater than the scaling parameter in gravitational term:

$$\frac{2V_p \left(\rho_s - \rho_l\right)}{C_D \rho_l A {v_s}^2} \frac{{\omega_s}^2}{r_s} \gg \frac{2V_p \left(\rho_s - \rho_l\right) g}{C_D \rho_l A {v_s}^2} \tag{6.16}$$

By canceling out the common terms in the above inequality:

$$\frac{{\omega_s}^2}{r_s g} \gg 1 \tag{6.17}$$

r_s is the tank radius, g is the gravitational acceleration, and ω_s is the angular velocity which is given by:

$$\omega_s = D_i N_i \tag{6.18}$$

Where D_i is the impeller diameter and N_i is the rotational rate (RPS). By solving Eqn (6.17) for the presented system, the rotational rate at which the effect of centrifugal force on a particle is greater than gravitational force is 207 RPM.

Figure 6.10 shows the hydrostatic pressure profile at 60 RPM, $\alpha_d = 0.10$. Due to the small scale of the tank, the hydrostatic pressure does not change much in the XZ-plane. However, a peak in pressure is observed around the outer walls as the moving fluid around the impeller hits the baffles. The pressure around the impeller is observed in the XY-plane cross-section. As expected, the pressure in front of the blades is greater than the pressure behind them as they force the front-side fluid to move and leave a void behind (pressure drop).

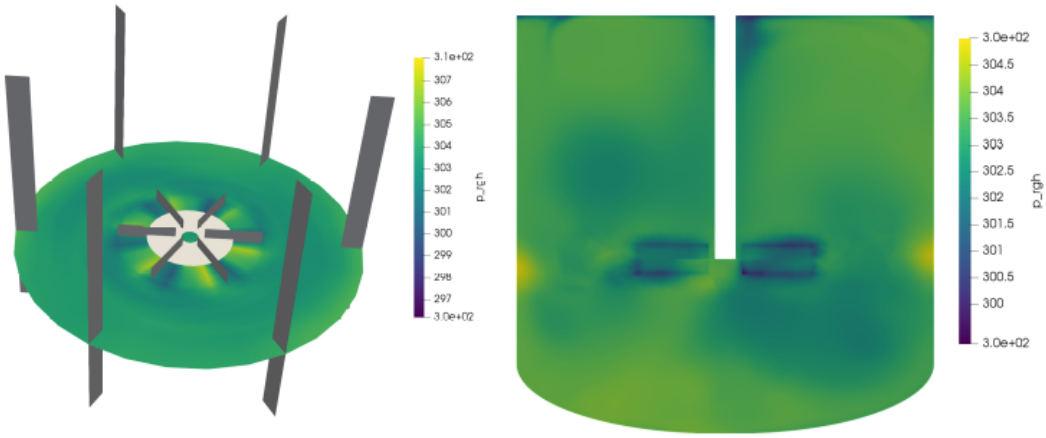

Figure 6.10: Hydrostatic pressure profile with cross-section in XY-plane (left) and cross-section in XZ-plane (left). At 60 RPM - 200 sec. Colors represent hydrostatic pressure.

6.4 Power Number Calculation and Validation

Power consumption is one of the most common approaches to validate a CFD model in agitated tanks [83]. Computationally, the power consumption, P, is determined from the torque applied by the impeller to its surrounding fluid [83]:

$$P = 2\pi N M_z \tag{6.19}$$

Where N is the impeller rotations per unit time (sec) and M_z denotes the axial component, i.e., the axis of rotation (z-direction), of vector M. M is the overall moment of the stress force, also known as torque:

$$M = \int_{A_I} \mathbf{r} \times (\boldsymbol{\pi} \cdot \mathbf{n})\, dA \tag{6.20}$$

A_I is the surface of the impeller blades, $\mathbf{r}$ is the position vector, $\mathbf{n}$ is the unit vector normal to the surface, and $\boldsymbol{\pi}$ is the stress tensor given by:

$$\boldsymbol{\pi} = p\mathbf{I} + \boldsymbol{\tau} \tag{6.21}$$

p is the dynamic pressure, $\mathbf{I}$ is the identity tensor and $\boldsymbol{\tau}$ is the stress deviator tensor of the fluid.

Figure 6.11 was employed as a reference to validate the achieved power number from simulation results. In this figure, the ungassed power number vs. impeller's Reynolds number in Newtonian fluids is plotted for different impeller designs. The "standard" geometrical ratios provided in Figure 6.2 were used for all the tested bioreactors in Reference [72]. It is reported that scaling up or down does not effect the power number-Reynolds number relationship as long as all the geometrical ratios stay the same [72]. Curve 1 represents the Rushton turbine impeller design and it is of interest here.

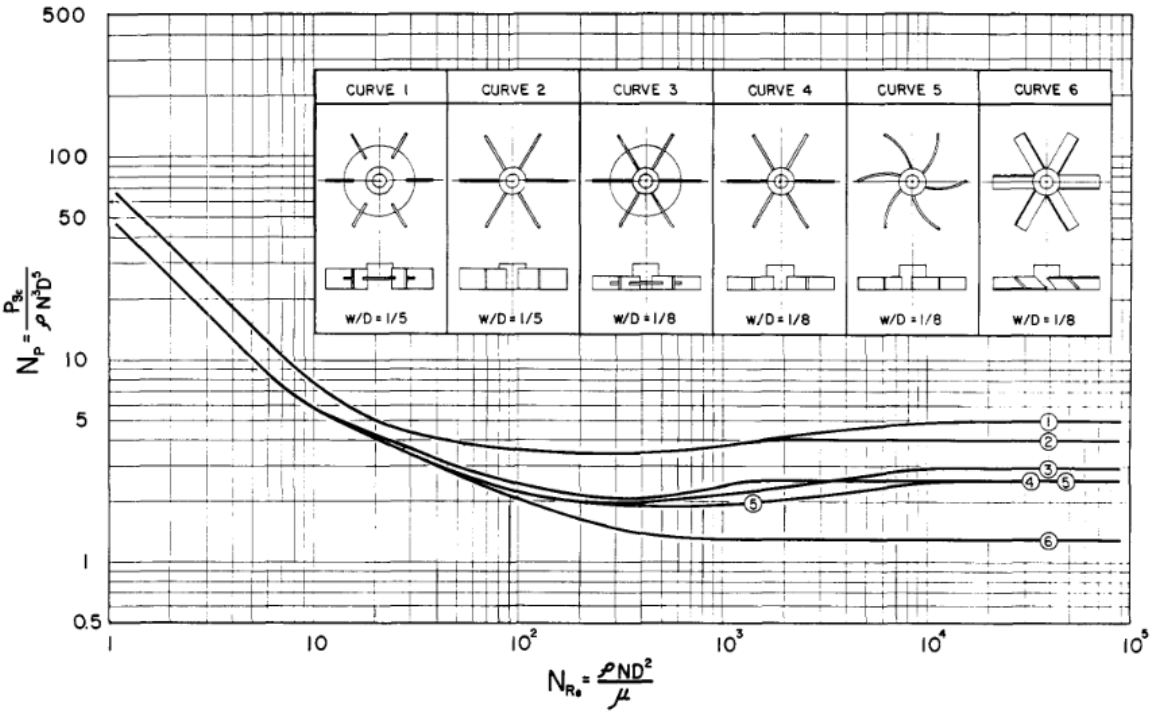

Figure 6.11: Ungassed power number vs. impeller Reynolds number for Newtonian fluids [72]. w is the width of the blades and D is the impeller diameter.

In order to have a better comparison between the computed power number and experiments, the proposed geometry in Section 6.1 was modified based on the "standard" condition bioreactor, see Figure 6.12. This bioreactor has a flat bottom with height to diameter ratio of 1 and four full-length baffles radially attached to its interior walls. A six-bladed Rushton turbine was mounted on the top of the tank. Table 6.3 shows the geometrical ratios in the modeled tank and the reference. Z is the liquid depth which here

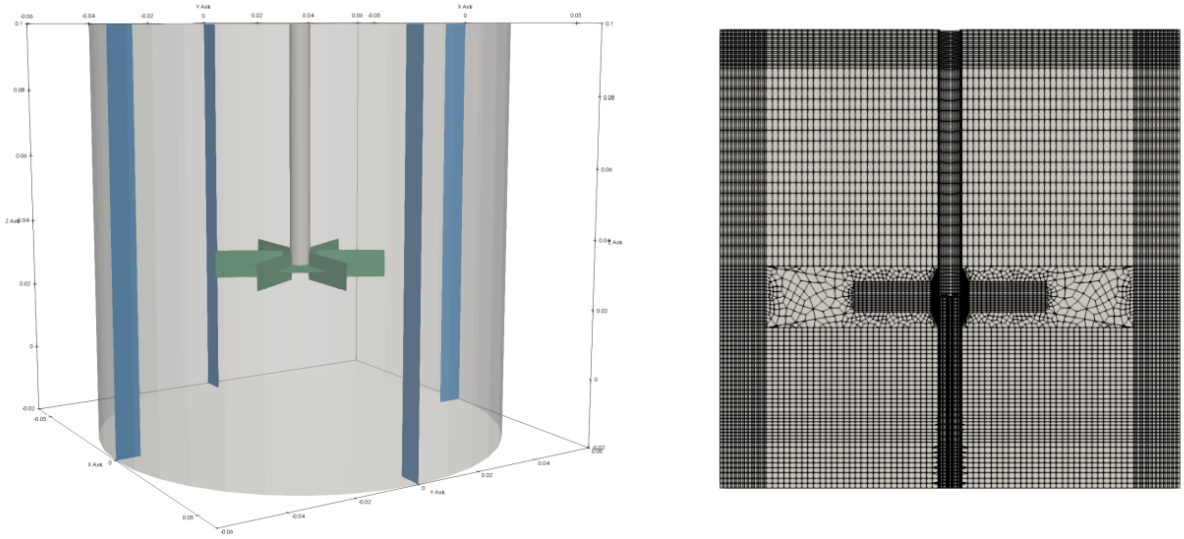

Figure 6.12: "Standard" condition bioreactor geometry and mesh.

is assumed to be the tank height, T is the diameter of the tank, D is the impeller diameter, C is the distance of the impeller from the bottom of the tank, n_b is the number of baffles, w_b is the width of the baffles and w is the width of the blades.

Table 6.3: Modeled geometry and "standard" geometry used in Ref. [72].

Ratios	Modeled Geometry	Geometry in Ref. [72]
Z/T	1	1
D/T	5/12	1/3
C/T	5/12	1/3
n_b	4	4
w_b	1/10	1/12
w/D	3/5	1/5

In this study, the torque value for each case was obtained using the `forces` function in `OpenFOAM`. The `forces` function generates moment data for impeller and blade surfaces by solving Eqn. (6.20). The moment data in the z-direction were extracted and plotted in Figure 6.13. This figure shows the impeller torque for different rotational rates at $\alpha_d = 0.10$. As expected, the torque mean increases with RPM.

To proceed with validation, the power number for each case in Figure 6.13 was calculated using Equations (6.19) and (2.25) for the average torque after reaching steady-state. The impeller Reynolds number, Re_i, is given in Eqn. (2.27) where ρ_l is substituted by the mixture density determined by Eqn. (2.18) and μ_l is substituted by the apparent mixture viscosity estimated by Eqn. (6.9).

Table 6.4: Power number and impeller Reynolds number values for 30 RPM, 60 RPM, and 90 RPM at $\alpha_d = 0.10$

	30 RPM	60 RPM	90 RPM
N_p	2.54	2.80	2.81
Re_i	1084.11	2168.23	3252.34

Table 6.4 shows the power number and impeller Reynolds number values for cases in Figure 6.13. Based on Figure 6.11 for the range of Reynolds number presented here, the power number should be in between 3 and 5. However, the calculated power numbers for the simulations are below that range. The underestimation of power number and overestimation of hindered settling velocity, presented in Section 5.1.2, have one common parameter, the apparent viscosity. Power number is the ratio of viscous forces to inertial. Therefore, underestimation of apparent viscosity results in lower power number. Moreover, as it was mentioned in Section 5.1.2, the settling velocity is inversely proportional to apparent viscosity and underestimation of apparent viscosity causes overestimation of settling velocity.

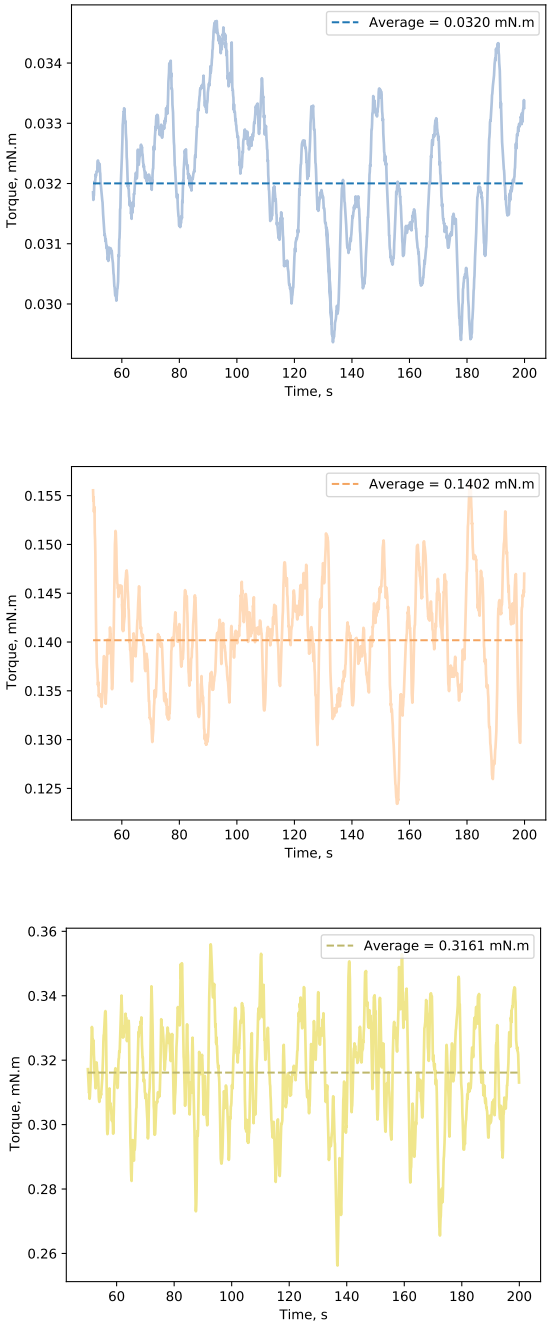

Figure 6.13: Torque vs time for 30 RPM (top), 60 RPM (middle), and 90 RPM (bottom).

Chapter 7

Conclusions and Future Work

7.1 Conclusions

In this work, a "hybrid" three-phase model for biological multi-phase flows is developed to enable the simulation of industrial-scale bioreactors. This model employs the drift-flux multi-phase model for liquid/dispersed solid portion of a biological flow and uses the two-fluid (Euler-Euler) model for the mixture-gas flow, where the mixture is the liquid/dispersed solid phase. The proposed multi-phase model reduces the computational complexity of a biological multi-phase flow simulation through reducing the number of partial differential equations that must be solved, without significant loss in accuracy compared to a three-phase Euler-Euler formulation.

In the drift-flux model, the diffusion velocity, $\boldsymbol{u}_{dm}$, captures the relative motion between the phases. By considering all the major acting forces on a particle inside an agitated bioreactor (centrifugal force, drag force, and buoyancy force), and Newton's second law of motion, Eqn. (6.10) was developed and implemented for the diffusion velocity. The diffusion velocity utilizes the apparent viscosity of the two-phase "mixture" determined from experimentation [13], Eqn. (6.9).

The "mixture" portion of the model was simulated inside a stirred tank bioreactor for three rotational speeds (30, 60, and 90 RPM) and three biomass concentrations ($\alpha_d = 0.01$, 0.05, and 0.10). The results were then validated against experiments for: 1) hindered settling velocity and 2) the impeller power number. The first validation showed decrease in hindered settling velocity by increase in volume fraction. This was in agreement with empirical results, however, an overestimation in the magnitude of settling velocity was observed. The second validation showed an underestimation of the computed power number. Power number and hindered settling velocity are both related to apparent viscosity. Power number is proportional to apparent viscosity as it is defined by the ratio of viscous forces to inertial. On the other hand, hindered settling

velocity is inversely proportional to apparent viscosity. By considering the estimation behaviour of the model and its relationship to apparent viscosity, one can conclude that maybe apparent viscosity was understated.

7.2 Future Work

The main set of recommendations for future work of this project are to complete the design of a simulation-based industrial-sized bioreactor. In order to achieve this goal, future work includes the following:

- **Implementation of the gas phase** - To complete a three-phase flow simulation, the gas phase should be added to the system through an inlet, possibly a sparger.
- **Implementation of mass transfer between the phases** - One of the most critical parameters in an aerobic bioprocess is the oxygen transfer rate and oxygen accessibility during an operation [36]. The oxygen transfer between the air bubble-medium and the medium-cell should be implemented. Additionally, the mass transfer between the medium-cell for nutrient transfer should also be implemented.
- **Implementation of metabolic reactions** - The performance of a bioreactor can be improved by leading the cell metabolism towards enhancement in yield, productivity, and selectivity of the outcome product [84].
- **High-density cell culture** - Only low concentrations of biomass ($\alpha_d \leq 0.10$) were studied in this work. Increasing the biomass load of a process can result in non-Newtonian fluid behavior, as shown in Figure 2.2. A viscosity model should be implemented to enable the simulations of high-density cultures that mimics Bingham pseudoplastic fluid behavior.

References

[1] H. Singh and D. W. Hutmacher. *Bioreactor Studies and Computational Fluid Dynamics*. Springer Berlin Heidelberg, Berlin, Heidelberg, 2009.

[2] Ryan Z Davis. Design and scale-up of production scale stirred tank fermentors. 2010.

[3] Brandy Sargent. Aeration and cell culture optimization in bioreactors.

[4] Treeratanaphitak, Tanyakarn. Diffuse solid-fluid interface method for dispersed multiphase flows, 2018.

[5] Daniel Brennan. *The numerical simulation of two phase flows in settling tanks*. PhD thesis, Imperial College London (University of London), 2001.

[6] A Lapin and A Lübbert. Numerical simulation of the dynamics of two-phase gas—liquid flows in bubble columns. *Chemical Engineering Science*, 49(21):3661–3674, 1994.

[7] G Montante, D Horn, and A Paglianti. Gas–liquid flow and bubble size distribution in stirred tanks. *Chemical engineering science*, 63(8):2107–2118, 2008.

[8] Woong Kim, Jennifer K Ng, Miki E Kunitake, Bruce R Conklin, and Peidong Yang. Interfacing silicon nanowires with mammalian cells. *Journal of the American Chemical Society*, 129(23):7228–7229, 2007.

[9] E Bourloutski and M Sommerfeld. Euler/lagrange calculations of gas-liquid-solid-flows in bubble columns with phase interaction. In *Bubbly Flows*, pages 243–259. Springer, 2004.

[10] Stefanie Brüning and Dirk Weuster-Botz. Cfd analysis of interphase mass transfer and energy dissipation in a milliliter-scale stirred-tank reactor for filamentous microorganisms. *Chemical Engineering Research and Design*, 92(2):240–248, 2014.

[11] Meenal S Puthli, Virendra K Rathod, and Aniruddha B Pandit. Gas–liquid mass transfer studies with triple impeller system on a laboratory scale bioreactor. *Biochemical Engineering Journal*, 23(1):25–30, 2005.

[12] Ricardo Gelves, A Dietrich, and Ralf Takors. Modeling of gas–liquid mass transfer in a stirred tank bioreactor agitated by a rushton turbine or a new pitched blade impeller. *Bioprocess and biosystems engineering*, 37(3):365–375, 2014.

[13] Andreea Iordan, Alain Duperray, and Claude Verdier. Fractal approach to the rheology of concentrated cell suspensions. *Physical Review E*, 77(1):011911, 2008.

[14] Marcus Reiner. Rheology. In *Elasticity and Plasticity/Elastizität und Plastizität*, pages 434–550. Springer, 1958.

[15] Herman F George and Farrukh Qureshi. Newton's law of viscosity, newtonian and non-newtonian fluids. *Encyclopedia of Tribology*, pages 2416–2420, 2013.

[16] Ronald Darby, Ron Darby, and Raj P Chhabra. *Chemical engineering fluid mechanics, revised and expanded*. CRC Press, 2017.

[17] SM Richardson. Non-newtonian fluids. *Thermopedia, doi*, 10, 2000.

[18] S Mueller, EW Llewellin, and HM Mader. The rheology of suspensions of solid particles. *Proceedings of the Royal Society A: Mathematical, Physical and Engineering Sciences*, 466(2116):1201–1228, 2010.

[19] Irvin M Krieger and Thomas J Dougherty. A mechanism for non-newtonian flow in suspensions of rigid spheres. *Transactions of the Society of Rheology*, 3(1):137–152, 1959.

[20] P Coussot. Introduction to the rheology of complex fluids. In *Understanding the rheology of concrete*, pages 3–22. Elsevier, 2012.

[21] Lutz Heymann, Sigrid Peukert, and Nuri Aksel. On the solid-liquid transition of concentrated suspensions in transient shear flow. *Rheologica acta*, 41(4):307–315, 2002.

[22] Multiphase Flow Handbook. Ct crowe, 2006.

[23] Mamoru Ishii and Takashi Hibiki. *Thermo-fluid dynamics of two-phase flow*. Springer Science & Business Media, 2010.

[24] S Elghobashi and GC Truesdell. On the two-way interaction between homogeneous turbulence and dispersed solid particles. i: Turbulence modification. *Physics of Fluids A: Fluid Dynamics*, 5(7):1790–1801, 1993.

[25] Donald A Drew and Stephen L Passman. *Theory of multicomponent fluids*, volume 135. Springer Science & Business Media, 2006.

[26] David Paul Hill. *The computer simulation of dispersed two-phase flow*. PhD thesis, Citeseer, 1998.

[27] Paulo J Oliveira and Raad I Issa. On the numerical treatment of interphase forces in two-phase flow. *ASME-PUBLICATIONS-FED*, 185:131–131, 1994.

[28] Chao Yang and Zai-Sha Mao. *Numerical simulation of multiphase reactors with continuous liquid phase*. Academic Press, 2014.

[29] A Eugene Raj and N Ganesh Karanth. 03 fermentation technology and bioreactor design. In *Food Biotechnology*, pages 60–113. CRC Press, 2005.

[30] Meriem Ammar, Zied Driss, Wajdi Chtourou, and Mohamed Abid. Effects of baffle length on turbulent flows generated in stirred vessels. *Open Engineering*, 1(4):401–412, 2011.

[31] R Byron Bird. Transport phenomena. *Appl. Mech. Rev.*, 55(1):R1–R4, 2002.

[32] K Hanjalic. Closure models for incompressible turbulent flows. *Lecture Notes at Von Kármán Institute*, 75, 2004.

[33] Minghui Xie, Jianye Xia, Zhen Zhou, Ju Chu, Yingping Zhuang, and Siliang Zhang. Flow pattern, mixing, gas hold-up and mass transfer coefficient of triple-impeller configurations in stirred tank bioreactors. *Industrial & Engineering Chemistry Research*, 53(14):5941–5953, 2014.

[34] Karl Schügerl. Development of bioreaction engineering. In *History of Modern Biotechnology II*, pages 41–76. Springer, 2000.

[35] NMG Oosterhuis and NWF Kossen. Power input measurements in a production scale bioreactor. *Biotechnology Letters*, 3(11):645–650, 1981.

[36] Sören Werner, Stephan C Kaiser, Matthias Kraume, and Dieter Eibl. Computational fluid dynamics as a modern tool for engineering characterization of bioreactors. *Pharmaceutical Bioprocessing*, 2(1):85–99, 2014.

[37] JA Sánchez Pérez, EM Rodríguez Porcel, JL Casas López, JM Fernández Sevilla, and Y Chisti. Shear rate in stirred tank and bubble column bioreactors. *Chemical Engineering Journal*, 124(1-3):1–5, 2006.

[38] P Bonvillani, MP Ferrari, EM Ducrós, and JA Orejas. Theoretical and experimental study of the effects of scale-up on mixing time for a stirred-tank bioreactor. *Brazilian Journal of Chemical Engineering*, 23(1):1–7, 2006.

[39] Christian Löffelholz, Stephan C Kaiser, Matthias Kraume, Regine Eibl, and Dieter Eibl. Dynamic single-use bioreactors used in modern liter-and m 3-scale biotechnological processes: engineering characteristics and scaling up. In *Disposable Bioreactors II*, pages 1–44. Springer, 2013.

[40] A-I Galaction, Dan Cascaval, Corneliu Oniscu, and Marius Turnea. Prediction of oxygen mass transfer coefficients in stirred bioreactors for bacteria, yeasts and fungus broths. *Biochemical Engineering Journal*, 20(1):85–94, 2004.

[41] Pierre-Alain Ruffieux, Urs von Stockar, and Ian William Marison. Measurement of volumetric (our) and determination of specific (qo2) oxygen uptake rates in animal cell cultures. *Journal of biotechnology*, 63(2):85–95, 1998.

[42] Petar Liovic, Ilija D Šutalo, Laurence Meagher, and George O Lovrecz. Computations of flow environments in medium-scale stirred-tank bioreactors for stem cell expansion. In *Fluids Engineering Division Summer Meeting*, volume 46247, page V01DT26A005. American Society of Mechanical Engineers, 2014.

[43] Alexei Lapin, Dirk Müller, and Matthias Reuss. Dynamic behavior of microbial populations in stirred bioreactors simulated with euler- lagrange methods: Traveling along the lifelines of single cells. *Industrial & engineering chemistry research*, 43(16):4647–4656, 2004.

[44] Alexei Lapin, Joachim Schmid, and Matthias Reuss. Modeling the dynamics of e. coli populations in the three-dimensional turbulent field of a stirred-tank bioreactor—a structured–segregated approach. *Chemical engineering science*, 61(14):4783–4797, 2006.

[45] Jie Ding, Xu Wang, Xue-Fei Zhou, Nan-Qi Ren, and Wan-Qian Guo. Cfd optimization of continuous stirred-tank (cstr) reactor for biohydrogen production. *Bioresource technology*, 101(18):7005–7013, 2010.

[46] Angélique Delafosse, Céline Loubière, Sébastien Calvo, Dominique Toye, and Eric Olmos. Solid-liquid suspension of microcarriers in stirred tank bioreactor–experimental and numerical analysis. *Chemical Engineering Science*, 180:52–63, 2018.

[47] Cyril W Hirt and Billy D Nichols. Volume of fluid (vof) method for the dynamics of free boundaries. *Journal of computational physics*, 39(1):201–225, 1981.

[48] Grétar Tryggvason, Ruben Scardovelli, and Stéphane Zaleski. *Direct numerical simulations of gas–liquid multiphase flows*. Cambridge University Press, 2011.

[49] John C Lamont and DS Scott. An eddy cell model of mass transfer into the surface of a turbulent liquid. *AIChE Journal*, 16(4):513–519, 1970.

[50] Jean d'Ans and Ellen Lax. *Taschenbuch für Chemiker und Physiker*. Springer-Verlag, 2013.

[51] Lewis Fry Richardson and J Arthur Gaunt. Viii. the deferred approach to the limit. *Philosophical Transactions of the Royal Society of London. Series A, containing papers of a mathematical or physical character*, 226(636-646):299–361, 1927.

[52] Yoshinori Kawase, Benoit Halard, and Murray Moo-Young. Liquid-phase mass transfer coefficients in bioreactors. *Biotechnology and bioengineering*, 39(11):1133–1140, 1992.

[53] Marko Laakkonen, Ville Alopaeus, and Juhani Aittamaa. Validation of bubble breakage, coalescence and mass transfer models for gas–liquid dispersion in agitated vessel. *Chemical engineering science*, 61(1):218–228, 2006.

[54] David Ting. *Basics of engineering turbulence*. Academic Press, 2016.

[55] Deqiang Li, Tingting Tang, Jianxi Lu, and Kerong Dai. Effects of flow shear stress and mass transport on the construction of a large-scale tissue-engineered bone in a perfusion bioreactor. *Tissue Engineering Part A*, 15(10):2773–2783, 2009.

[56] Badie I Morsi and Omar M Basha. Mass transfer in multiphase systems. *Mass transfer-advancement in process modelling. InTech*, pages 189–217, 2015.

[57] Valentin Jossen, Stephan C Kaiser, Carmen Schirmaier, Jacqueline Herrmann, Dieter Eibl, Ann Siehoff, Christian van den Bos, Regine Eibl, et al. Modification and qualification of a stirred single-use bioreactor for the improved expansion of human mesenchymal stem cells at benchtop scale. *Pharmaceutical Bioprocessing*, 2(4):311–322, 2014.

[58] Mo Syamlal. The particle-particle drag term in a multiparticle model of fluidization. Technical report, EG and G Washington Analytical Services Center, Inc., Morgantown, WV (USA), 1987.

[59] Guan Heng Yeoh and Jiyuan Tu. *Computational techniques for multiphase flows*. Butterworth-Heinemann, 2019.

[60] Christopher Earls Brennen and Christopher E Brennen. *Fundamentals of multiphase flow*. Cambridge university press, 2005.

[61] Nian-Sheng Cheng. Comparison of formulas for drag coefficient and settling velocity of spherical particles. *Powder Technology*, 189(3):395–398, 2009.

[62] DA Drew and RT Lahey Jr. The virtual mass and lift force on a sphere in rotating and straining inviscid flow. *International Journal of Multiphase Flow*, 13(1):113–121, 1987.

[63] Alexande Sokolichin, Gerhart Eigenberger, and Alexej Lapin. Simulation of buoyancy driven bubbly flow: established simplifications and open questions. *AIChE Journal*, 50(1):24–45, 2004.

[64] Jyeshtharaj Joshi and Arun K Nayak. *Advances of computational fluid Dynamics in nuclear reactor design and safety assessment*. Woodhead Publishing, 2019.

[65] SP Antal, RT Lahey Jr, and JE Flaherty. Analysis of phase distribution in fully developed laminar bubbly two-phase flow. *International journal of multiphase flow*, 17(5):635–652, 1991.

[66] Manotosh Kumbhakar, Snehasis Kundu, and Koeli Ghoshal. Hindered settling velocity in particle-fluid mixture: a theoretical study using the entropy concept. *Journal of Hydraulic Engineering*, 143(11):06017019, 2017.

[67] Subhasish Dey, Sk Zeeshan Ali, and Ellora Padhi. Terminal fall velocity: the legacy of stokes from the perspective of fluvial hydraulics. *Proceedings of the Royal Society A*, 475(2228):20190277, 2019.

[68] Kiley Benes, Penger Tong, and Bruce J Ackerson. Sedimentation, péclet number, and hydrodynamic screening. *Physical Review E*, 76(5):056302, 2007.

[69] D Bruneau, R Anthore, F Feuillebois, X Auvray, and C Petipas. Measurement of the average velocity of sedimentation in a dilute polydisperse suspension of spheres. *Journal of fluid mechanics*, 221:577–596, 1990.

[70] MA Al-Naafa and M Sami Selim. Sedimentation of monodisperse and bidisperse hard-sphere colloidal suspensions. *AIChE Journal*, 38(10):1618–1630, 1992.

[71] Elisabetta Del Bello, Jacopo Taddeucci, Mattia de'Michieli Vitturi, Piergiorgio Scarlato, Daniele Andronico, Simona Scollo, Ulrich Kueppers, and Tullio Ricci. Effect of particle volume fraction on the settling velocity of volcanic ash particles: insights from joint experimental and numerical simulations. *Scientific reports*, 7:39620, 2017.

[72] Robert L Bates, Philip L Fondy, and Robert R Corpstein. Examination of some geometric parameters of impeller power. *Industrial & Engineering Chemistry Process Design and Development*, 2(4):310–314, 1963.

[73] Mahsa Taghavi, Ramin Zadghaffari, Jafarsadegh Moghaddas, and Yousef Moghaddas. Experimental and cfd investigation of power consumption in a dual rushton turbine stirred tank. *Chemical Engineering Research and Design*, 89(3):280–290, 2011.

[74] G.Vijay Chithra. Power requirements for mixing in bioreactors, 2019.

[75] Andrea K Bryan, Vivian C Hecht, Wenjiang Shen, Kristofor Payer, William H Grover, and Scott R Manalis. Measuring single cell mass, volume, and density with dual suspended microchannel resonators. *Lab on a Chip*, 14(3):569–576, 2014.

[76] The OpenFOAM Foundation. Openfoam user guide v2006, 2006.

[77] Guiguer, Victor. Iterative coupled shell/tube simulation of waste heat boilers using computational multiphysics, 2019.

[78] Christophe Geuzaine and Jean-François Remacle. Gmsh: A 3-d finite element mesh generator with built-in pre-and post-processing facilities. *International journal for numerical methods in engineering*, 79(11):1309–1331, 2009.

[79] The OpenFOAM Foundation. Openfoam v6 user guide, 2017.

[80] Fadl Moukalled, L Mangani, Marwan Darwish, et al. *The finite volume method in computational fluid dynamics*, volume 6. Springer, 2016.

[81] Brecht Devolder, Pál Schmitt, Pieter Rauwoens, Björn Elsaesser, and Peter Troch. A review of the implicit motion solver algorithm in openfoam® to simulate a heaving buoy. In *NUTTS conference*, volume 2015, page 18th, 2015.

[82] Rouzbeh Jafari, Philippe A Tanguy, and Jamal Chaouki. Characterization of minimum impeller speed for suspension of solids in liquid at high solid concentration, using gamma-ray densitometry. *International Journal of Chemical Engineering*, 2012, 2012.

[83] Marti Cortada-Garcia, Valentina Dore, Luca Mazzei, and Panagiota Angeli. Experimental and cfd studies of power consumption in the agitation of highly viscous shear thinning fluids. *Chemical Engineering Research and Design*, 119:171–182, 2017.

[84] Thiago José Barbosa Mesquita, Cíntia Regina Sargo, José Roberto Fuzer, Sheyla Alexandra Hidalgo Paredes, Roberto de Campos Giordano, Antonio Carlos Luperni Horta, and Teresa Cristina Zangirolami. Metabolic fluxes-oriented control of bioreactors: a novel approach to tune micro-aeration and substrate feeding in fermentations. *Microbial cell factories*, 18(1):1–17, 2019.

[85] Ralf Pörtner, Stephanie Nagel-Heyer, Christiane Goepfert, Peter Adamietz, and Norbert M Meenen. Bioreactor design for tissue engineering. *Journal of bioscience and bioengineering*, 100(3):235–245, 2005.

[86] Simon Judd. The status of membrane bioreactor technology. *Trends in biotechnology*, 26(2):109–116, 2008.

[87] JC Merchuk, A Contreras, F Garcia, and E Molina. Studies of mixing in a concentric tube airlift bioreactor with different spargers. *Chemical Engineering Science*, 53(4):709–719, 1998.

[88] Regine Eibl and Dieter Eibl. *Single-use technology in biopharmaceutical manufacture*. John Wiley & Sons, 2011.

[89] Zhiyi Yu, Baoshan Zhu, Shuliang Cao, and Ying Liu. Effect of virtual mass force on the mixed transport process in a multiphase rotodynamic pump. *Advances in Mechanical Engineering*, 6:958352, 2014.

[90] Yusuf Chisti. Animal cell culture in stirred bioreactors: observations on scale-up. *Bioprocess Engineering*, 9(5):191–196, 1993.

[91] TG Theofanous, RN Houze, and LK Brumfield. Turbulent mass transfer at free, gas-liquid interfaces, with applications to open-channel, bubble and jet flows. *International Journal of Heat and Mass Transfer*, 19(6):613–624, 1976.

[92] TG Theofanous. The boiling crisis in nuclear reactor safety and performance. *International Journal of Multiphase Flow*, 6(1-2):69–95, 1980.

[93] F Bezzo, S Macchietto, and CC Pantelides. General hybrid multizonal/cfd approach for bioreactor modeling. *AIChE Journal*, 49(8):2133–2148, 2003.

[94] Hamidreza Azargoshasb, Seyyed Mohammad Mousavi, Oveis Jamialahmadi, Seyed Abbas Shojaosadati, and Seyyed Babak Mousavi. Experiments and a three-phase computational fluid dynamics (cfd) simulation coupled with population balance equations of a stirred tank bioreactor for high cell density cultivation. *The Canadian Journal of Chemical Engineering*, 94(1):20–32, 2016.

[95] Kumar Dhanasekharan. Design and scale-up of bioreactors using computer simulations. *BioProcess Int*, 4(3), 2006.

[96] Shankar Subramaniam. Lagrangian–eulerian methods for multiphase flows. *Progress in Energy and Combustion Science*, 39(2-3):215–245, 2013.

[97] E Bourloutski and M Sommerfeld. Transient euler/lagrange calculations of dense gas-liquid-solid-flows in bubble columns with consideration of phase interaction. In *Proceedings 10th Workshop on Two-Phase Flow Predictions, Merseburg*, pages 113–123, 2002.

[98] M Sommerfeld. Theoretical and experimental modelling of particulate flows. *Lecture series*, 6:3–7, 2000.

[99] Mikko Manninen, Veikko Taivassalo, Sirpa Kallio, et al. On the mixture model for multiphase flow, 1996.

[100] Ralf Hortsch, Ansgar Stratmann, and Dirk Weuster-Botz. New milliliter-scale stirred tank bioreactors for the cultivation of mycelium forming microorganisms. *Biotechnology and bioengineering*, 106(3):443–451, 2010.

[101] MA Rizk and SE Elghobashi. A two-equation turbulence model for dispersed dilute confined two-phase flows. *International Journal of Multiphase Flow*, 15(1):119–133, 1989.

[102] R Israel and Daniel E Rosner. Use of a generalized stokes number to determine the aerodynamic capture efficiency of non-stokesian particles from a compressible gas flow. *Aerosol Science and Technology*, 2(1):45–51, 1982.

[103] Joanna Karcz and Marta Major. An effect of a baffle length on the power consumption in an agitated vessel. *Chemical Engineering and Processing: Process Intensification*, 37(3):249–256, 1998.

[104] Ali Karimi, Farideh Golbabaei, Momammad Reza Mehrnia, Masoud Neghab, Kazem Mohammad, Ahmad Nikpey, and Mohammad Reza Pourmand. Oxygen mass transfer in a stirred tank bioreactor using different impeller configurations for environmental purposes. *Iranian journal of environmental health science & engineering*, 10(1):6, 2013.

[105] Nicolò Falcone, Andrea Bersano, Cristina Bertani, Mario De Salve, and Bruno Panella. Characterization of water-air dispersed two phase flow. *Energy Procedia*, 126:66–73, 2017.

[106] Marco Jose Da Silva. Impedance sensors for fast multiphase flow measurement and imaging. 2008.

[107] Pinchas Doron and Dvora Barnea. Flow pattern maps for solid-liquid flow in pipes. *International journal of multiphase flow*, 22(2):273–283, 1996.

[108] Ramin Dabirian, Ram Mohan, Ovadia Shoham, and Gene Kouba. Critical sand deposition velocity for gas-liquid stratified flow in horizontal pipes. *Journal of Natural Gas Science and Engineering*, 33:527–537, 2016.

[109] Shu Chien, SHUNICHI Usami, Harry M Taylor, John L Lundberg, and Magnus I Gregersen. Effects of hematocrit and plasma proteins on human blood rheology at low shear rates. *Journal of Applied Physiology*, 21(1):81–87, 1966.

[110] Lutz Heymann, Sigrid Peukert, and Nuri Aksel. Investigation of the solid–liquid transition of highly concentrated suspensions in oscillatory amplitude sweeps. *Journal of Rheology*, 46(1):93–112, 2002.

[111] Randall J LeVeque et al. *Finite volume methods for hyperbolic problems*, volume 31. Cambridge university press, 2002.

[112] Stephan C Kaiser, Sören Werner, Valentin Jossen, Katharina Blaschczok, and Dieter Eibl. Power input measurements in stirred bioreactors at laboratory scale. *JoVE (Journal of Visualized Experiments)*, (135):e56078, 2018.

[113] Ideen Sadrehaghighi. Multiphase flow.

Appendix A

Derivation of the Drift Flux Model From the Euler-Euler Model

A.1 Mixture Continuity Equation

In the Euler-Euler model there is a continuity equation for each phase [23]:

$$\frac{\partial(\alpha_1\rho_1)}{\partial t} + \nabla \cdot (\alpha_1\rho_1\boldsymbol{u}_1) = 0 \tag{A.1}$$

$$\frac{\partial(\alpha_2\rho_2)}{\partial t} + \nabla \cdot (\alpha_2\rho_2\boldsymbol{u}_2) = 0 \tag{A.2}$$

Adding the two above equations will result in:

$$\frac{\partial(\alpha_1\rho_1 + \alpha_2\rho_2)}{\partial t} + \nabla \cdot (\alpha_1\rho_1\boldsymbol{u}_1 + \alpha_2\rho_2\boldsymbol{u}_2) = 0 \tag{A.3}$$

By Ishii's definition we have [23]:

$$\rho_m = \alpha_1\rho_1 + \alpha_2\rho_2 \tag{A.4}$$

$$\boldsymbol{u}_1 = \boldsymbol{u}_{1m} + \boldsymbol{u}_m \tag{A.5}$$

$$\boldsymbol{u}_2 = \boldsymbol{u}_{2m} + \boldsymbol{u}_m \tag{A.6}$$

$$\boldsymbol{u}_m = \frac{\alpha_c\rho_c\boldsymbol{u}_c + \alpha_d\rho_d\boldsymbol{u}_d}{\rho_m} \tag{A.7}$$

$$\alpha_1\rho_1\boldsymbol{u}_{1m} + \alpha_2\rho_2\boldsymbol{u}_{2m} = 0 \tag{A.8}$$

Where α_1 and α_2 are the volume fraction of phase 1 and phase 2, ρ_1 and ρ_2 are the density of phase 1 and phase 2, $\boldsymbol{u}_1$ and $\boldsymbol{u}_2$ are the velocity of phase 1 and phase 2, ρ_m is the mixture density, $\boldsymbol{u}_m$ is the mixture velocity and $\boldsymbol{u}_{1m}$ and $\boldsymbol{u}_{2m}$ are the diffusion velocity of phase 1 and phase 2 respectively.
By substituting equations (A.5) and (A.6) in the second term of equation (A.3) we will have:

$$\alpha_1\rho_1\boldsymbol{u}_1 + \alpha_2\rho_2\boldsymbol{u}_2 = \alpha_1\rho_1 u_{1m} + \alpha_1\rho_1\boldsymbol{u}_m + \alpha_2\rho_2\boldsymbol{u}_{2m} + \alpha_2\rho_2\boldsymbol{u}_m \tag{A.9}$$

By factoring out $\boldsymbol{u}_m$ and using equations (A.4) and (A.8), the above equation will be:

$$\alpha_1\rho_1\boldsymbol{u}_1 + \alpha_2\rho_2\boldsymbol{u}_2 = (\alpha_1\rho_1 + \alpha_2\rho_2)\boldsymbol{u}_m = \rho_m\boldsymbol{u}_m \tag{A.10}$$

Hence the continuity equation is [23]:

$$\frac{\partial\rho_m}{\partial t} + \nabla\cdot(\rho_m\boldsymbol{u}_m) = 0 \tag{A.11}$$

A.2 Mixture Momentum Equation

The momentum equation for each phase in the Euler-Euler model is [23]:

$$\frac{\partial(\alpha_1\rho_1\boldsymbol{u}_1)}{\partial t} + \nabla\cdot(\alpha_1\rho_1\boldsymbol{u}_1\boldsymbol{u}_1) = -\nabla(\alpha_1 P_1) + \nabla\cdot(\alpha_1\boldsymbol{\tau}_1) + \alpha_1\rho_1\boldsymbol{g} + \mathbf{M}_1 \tag{A.12}$$

$$\frac{\partial(\alpha_2\rho_2\boldsymbol{u}_2)}{\partial t} + \nabla\cdot(\alpha_2\rho_2\boldsymbol{u}_2\boldsymbol{u}_2) = -\nabla(\alpha_2 P_2) + \nabla\cdot(\alpha_2\boldsymbol{\tau}_2) + \alpha_2\rho_2\boldsymbol{g} + \mathbf{M}_2 \tag{A.13}$$

By summing the above equations and using equation (A.10) the time derivative term on the right hand side becomes:

$$\frac{\partial(\alpha_1\rho_1\boldsymbol{u}_1)}{\partial t} + \frac{\partial(\alpha_2\rho_2\boldsymbol{u}_2)}{\partial t} = \frac{\partial(\alpha_1\rho_1\boldsymbol{u}_1 + \alpha_2\rho_2\boldsymbol{u}_2)}{\partial t} = \frac{\partial\rho_m\boldsymbol{u}_m}{\partial t} \tag{A.14}$$

By substituting $\boldsymbol{u}_1$ from equation (A.5) and $\boldsymbol{u}_2$ from equation (A.6) into the mixture momentum equation, the remaining term on the right hand side becomes:

$$\nabla\cdot(\alpha_1\rho_1\boldsymbol{u}_1\boldsymbol{u}_1)+\nabla\cdot(\alpha_2\rho_2\boldsymbol{u}_2\boldsymbol{u}_2) = \nabla\cdot(\alpha_1\rho_1[{u_{1m}}^2+2\boldsymbol{u}_{1m}\boldsymbol{u}_m+{u_m}^2]+\alpha_2\rho_2[{u_{2m}}^2+2\boldsymbol{u}_{2m}\boldsymbol{u}_m+{u_m}^2]) \tag{A.15}$$

Collecting terms:

$$= \alpha_1\rho_1 {u_{1m}}^2 + \alpha_2\rho_2 {u_{2m}}^2 + 2[\alpha_1\rho_1\boldsymbol{u}_{1m} + \alpha_2\rho_2\boldsymbol{u}_{2m}]\boldsymbol{u}_m + [\alpha_1\rho_1 + \alpha_2\rho_2]{u_m}^2 \tag{A.16}$$

Using (A.4) and (A.8):

$$= \alpha_1\rho_1\boldsymbol{u}_{1m}\boldsymbol{u}_{1m} + \alpha_2\rho_2\boldsymbol{u}_{2m}\boldsymbol{u}_{2m} + \rho_m\boldsymbol{u}_m\boldsymbol{u}_m = \Sigma\alpha_k\rho_k\boldsymbol{u}_{km}\boldsymbol{u}_{km} + \rho_m\boldsymbol{u}_m\boldsymbol{u}_m \tag{A.17}$$

In order to write the mixture momentum equation in terms of the drift velocity $\boldsymbol{u}_{kj}$, $\boldsymbol{u}_{km}$ needs to be replaced. By using equations (A.4), (A.5), (A.7), (A.8), and assuming k to be the dispersed phase (phase 2), we have:

$$\boldsymbol{u}_{2m} = -\frac{\alpha_1\rho_1}{\alpha_2\rho_2}\boldsymbol{u}_{1m} = -\frac{\alpha_1\rho_1}{\alpha_2\rho_2}(\boldsymbol{u}_1 - \boldsymbol{u}_m) = -\frac{\alpha_1\rho_1}{\alpha_2\rho_2}(\boldsymbol{u}_1 - \frac{\alpha_1\rho_1\boldsymbol{u}_1 + \alpha_2\rho_2\boldsymbol{u}_2}{\rho_m}) = -\frac{\alpha_1\rho_1}{\rho_m}(\boldsymbol{u}_1 - \boldsymbol{u}_2) \tag{A.18}$$

Drift velocity is defined as:

$$\boldsymbol{u}_{2j} = \alpha_1 \underbrace{(\boldsymbol{u}_2 - \boldsymbol{u}_1)}_{\boldsymbol{u}_r} = \alpha_1\boldsymbol{u}_r \tag{A.19}$$

By substituting the above equation into equation (A.18), we get to:

$$\boldsymbol{u}_{2m} = \frac{\rho_1}{\rho_m}\boldsymbol{u}_{2j} \tag{A.20}$$

The same calculation applies to $\boldsymbol{u}_{1m}$:

$$\boldsymbol{u}_{1m} = -\frac{\alpha_2}{\alpha_1}\frac{\rho_2}{\rho_m}\boldsymbol{u}_{2j} \tag{A.21}$$

By using equations (A.19) and (A.20) instead of $\boldsymbol{u}_{km}$ in (A.18):

$$\alpha_1\rho_1\boldsymbol{u}_{1m}\boldsymbol{u}_{1m} + \alpha_2\rho_2\boldsymbol{u}_{2m}\boldsymbol{u}_{2m} = \alpha_1\rho_1\big(-\frac{\alpha_2}{\alpha_1}\frac{\rho_2}{\rho_m}\boldsymbol{u}_{2j}\big)^2 + \alpha_2\rho_2\big(\frac{\rho_1}{\rho_m}\boldsymbol{u}_{2j}\big)^2 \tag{A.22}$$

The negative sign in the first term on the right hand side becomes positive as it is squared. By collecting the common terms we get to:

$$= \frac{\alpha_2\rho_1\rho_2}{{\rho_m}^2}\ {u_{2j}}^2\ \big[\frac{\alpha_2\rho_2}{\alpha_1} + \rho_1\big] = \frac{\alpha_2\rho_1\rho_2}{{\rho_m}^2}\ {u_{2j}}^2\ \big[\frac{\alpha_2\rho_2}{\alpha_1} + \frac{\alpha_1\rho_1}{\alpha_1}\big] \tag{A.23}$$

In the above equation, based on (A.4), the term in the bracket is equivalent to ρ_m/α_1. Thus, we have:

$$\alpha_1\rho_1\boldsymbol{u}_{1m}\boldsymbol{u}_{1m} + \alpha_2\rho_2\boldsymbol{u}_{2m}\boldsymbol{u}_{2m} = \frac{\alpha_2\rho_1\rho_2}{{\rho_m}^2}\ {u_{2j}}^2\ \big[\frac{\rho_m}{\alpha_1}\big] = \frac{\alpha_2}{\alpha_1}\frac{\rho_1\rho_2}{\rho_m}\ {u_{2j}}^2 \tag{A.24}$$

Therefore, equation (A.17) turns into:

$$\nabla\cdot(\alpha_1\rho_1\boldsymbol{u}_1\boldsymbol{u}_1) + \nabla\cdot(\alpha_2\rho_2\boldsymbol{u}_2\boldsymbol{u}_2) = \nabla\cdot(\rho_m\boldsymbol{u}_m\boldsymbol{u}_m) + \nabla\cdot\big(\frac{\alpha_2}{\alpha_1}\frac{\rho_1\rho_2}{\rho_m}\ {u_{2j}}^2\big) \tag{A.25}$$

For the left hand side, by definition we have:

$$\alpha_1 \boldsymbol{\tau}_1 + \alpha_2 \boldsymbol{\tau}_2 = \boldsymbol{\tau}_m \tag{A.26}$$

By using (A.4) for the gravity term:

$$\alpha_1 \rho_1 \boldsymbol{g} + \alpha_2 \rho_2 \boldsymbol{g} = (\alpha_1 \rho_1 + \alpha_2 \rho_2)\boldsymbol{g} = \rho_m \boldsymbol{g} \tag{A.27}$$

The momentum transfer terms between the two phases are equal in value and opposite in direction, meaning:

$$\boldsymbol{M}_1 + \boldsymbol{M}_2 = 0 \tag{A.28}$$

Hence, the mixture momentum equation has the form of:

$$\frac{\partial \rho_m \boldsymbol{u}_m}{\partial t} + \nabla \cdot (\rho_m \boldsymbol{u}_m \boldsymbol{u}_m) = -\nabla \cdot P_m + \nabla \cdot \boldsymbol{\tau}_m - \nabla \cdot \Big(\frac{\alpha_2}{\alpha_1} \frac{\rho_1 \rho_2}{\rho_m} \boldsymbol{u}_{2j} \boldsymbol{u}_{2j} \Big) + \rho_m \boldsymbol{g} \tag{A.29}$$

A.3 Dispersed Phase Continuity Equation

As it has been mentioned, the continuity equation for the dispersed phase can be written in terms of:

$$\frac{\partial (\alpha_2 \rho_2)}{\partial t} + \nabla \cdot (\alpha_2 \rho_2 \boldsymbol{u}_2) = 0 \tag{A.30}$$

From equations (A.6) and (A.20) we have:

$$\boldsymbol{u}_2 = \boldsymbol{u}_{2m} + \boldsymbol{u}_m$$

$$\boldsymbol{u}_{2m} = \frac{\rho_1}{\rho_m} \boldsymbol{u}_{2j}$$

By substituting (A.20) into (A.6) we have:

$$\boldsymbol{u}_2 = \frac{\rho_1}{\rho_m} \boldsymbol{u}_{2j} + \boldsymbol{u}_m \tag{A.31}$$

Using the above equation in the dispersed phase continuity equation gives us:

$$\frac{\partial (\alpha_2 \rho_2)}{\partial t} + \nabla \cdot (\alpha_2 \rho_2 \frac{\rho_1}{\rho_m} \boldsymbol{u}_{2j} + \alpha_2 \rho_2 \boldsymbol{u}_m) = 0 \tag{A.32}$$

Thus, the continuity equation for the dispersed phase is:

$$\frac{\partial (\alpha_2 \rho_2)}{\partial t} + \nabla \cdot (\alpha_2 \rho_2 \boldsymbol{u}_m) = -\nabla \cdot (\frac{\alpha_2 \rho_2 \rho_1}{\rho_m} \boldsymbol{u}_{2j}) \tag{A.33}$$

Appendix B

Source Code

B.1 quadraticMixture.H Viscosity Model

```
/*---------------------------------------------------------------------------*\
  =========                 |
  \\      /  F ield         | OpenFOAM: The Open Source CFD Toolbox
   \\    /   O peration     | Website:  https://openfoam.org
    \\  /    A nd           | Copyright (C) 2014-2018 OpenFOAM Foundation
     \\/     M anipulation  |
-------------------------------------------------------------------------------
License
    This file is part of OpenFOAM.

    OpenFOAM is free software: you can redistribute it and/or modify it
    under the terms of the GNU General Public License as published by
    the Free Software Foundation, either version 3 of the License, or
    (at your option) any later version.

    OpenFOAM is distributed in the hope that it will be useful, but
    WITHOUT
    ANY WARRANTY; without even the implied warranty of MERCHANTABILITY or
    FITNESS FOR A PARTICULAR PURPOSE.  See the GNU General Public License
    for more details.

    You should have received a copy of the GNU General Public License
    along with OpenFOAM.  If not, see <http://www.gnu.org/licenses/>.

Class
    Foam::mixtureViscosityModels::quadraticMixture
```

```
26
27 Description
28     Thomas' viscosity correction for quadraticMixture.
29
30     References:
31     \verbatim
32         "Transport characteristics of suspension:
33          VIII. A note on the viscosity of Newtonian suspensions
34          of uniform spherical particles".
35          D.G. Thomas,
36          J. Colloid Sci. 20 (3), 1965, p267.
37     \endverbatim
38
39 SourceFiles
40     quadraticMixture.C
41
42 \*---------------------------------------------------------------------------*/
43
44 #ifndef quadratic_mixture_H
45 #define quadratic_mixture_H
46
47 #include "mixtureViscosityModel.H"
48 #include "dimensionedScalar.H"
49 #include "volFields.H"
50
51 // * * * * * * * * * * * * * * * * * * * * * * * * * * * * * * * * * * * * //
52
53 namespace Foam
54 {
55
56 class incompressibleTwoPhaseInteractingMixture;
57
58 namespace mixtureViscosityModels
59 {
60
61 /*---------------------------------------------------------------------------*\
62                       Class quadraticMixture Declaration
63 \*---------------------------------------------------------------------------*/
64
65 class quadraticMixture
66 :
67     public mixtureViscosityModel
68 {
69 protected:
70
```

```
71      // Protected data
72
73          //- quadraticMixture phase fraction
74          const volScalarField& alpha_;
75
76
77  public:
78
79      //- Runtime type information
80      TypeName("quadraticMixture");
81
82
83      // Constructors
84
85          //- Construct from components
86          quadraticMixture
87          (
88              const word& name,
89              const dictionary& viscosityProperties,
90              const volVectorField& U,
91              const surfaceScalarField& phi,
92              const word modelName=typeName
93          );
94
95
96      //- Destructor
97      ~quadraticMixture()
98      {}
99
100
101     // Member Functions
102
103         //- Return the mixture viscosity
104         //  given the viscosity of the continuous phase
105         tmp<volScalarField> mu(const volScalarField& muc) const;
106
107         //- Read transportProperties dictionary
108         bool read(const dictionary& viscosityProperties);
109 };
110
111
112 // * * * * * * * * * * * * * * * * * * * * * * * * * * * * * * * * * * * * * * * * * //
113
114 } // End namespace mixtureViscosityModels
115 } // End namespace Foam
```

```
116
117 //  * * * * * * * * * * * * * * * * * * * * * * * * * * * * * * * * * * * * * //
118
119 #endif
120
121 // ************************************************************************* //
```

B.2 quadraticMixture.C Viscosity Model

```
1  /*---------------------------------------------------------------------------*\
2    =========                 |
3    \\      /  F ield         | OpenFOAM: The Open Source CFD Toolbox
4     \\    /   O peration     | Website:  https://openfoam.org
5      \\  /    A nd           | Copyright (C) 2014-2018 OpenFOAM Foundation
6       \\/     M anipulation  |
7  -------------------------------------------------------------------------------
8  License
9      This file is part of OpenFOAM.
10
11     OpenFOAM is free software: you can redistribute it and/or modify it
12     under the terms of the GNU General Public License as published by
13     the Free Software Foundation, either version 3 of the License, or
14     (at your option) any later version.
15
16     OpenFOAM is distributed in the hope that it will be useful, but
       WITHOUT
17     ANY WARRANTY; without even the implied warranty of MERCHANTABILITY or
18     FITNESS FOR A PARTICULAR PURPOSE.  See the GNU General Public License
19     for more details.
20
21     You should have received a copy of the GNU General Public License
22     along with OpenFOAM.  If not, see <http://www.gnu.org/licenses/>.
23
24 \*---------------------------------------------------------------------------*/
25
26 #include "quadraticMixture.H"
27 #include "addToRunTimeSelectionTable.H"
28
29 // * * * * * * * * * * * * * Static Data Members * * * * * * * * * * * * * //
30
31 namespace Foam
32 {
33 namespace mixtureViscosityModels
34 {
```

```
35      defineTypeNameAndDebug(quadraticMixture, 0);
36
37      addToRunTimeSelectionTable
38      (
39          mixtureViscosityModel,
40          quadraticMixture,
41          dictionary
42      );
43  }
44  }
45
46
47  // * * * * * * * * * * * * * * Constructors * * * * * * * * * * * * * * * //
48
49  Foam::mixtureViscosityModels::quadraticMixture::quadraticMixture
50  (
51      const word& name,
52      const dictionary& viscosityProperties,
53      const volVectorField& U,
54      const surfaceScalarField& phi,
55      const word modelName
56  )
57  :
58      mixtureViscosityModel(name, viscosityProperties, U, phi),
59      alpha_
60      (
61          U.mesh().lookupObject<volScalarField>
62          (
63              IOobject::groupName
64              (
65                  viscosityProperties.lookupOrDefault<word>("alpha", "alpha
    "),
66                  viscosityProperties.dictName()
67              )
68          )
69      )
70  {}
71
72
73  // * * * * * * * * * * * * * * Member Functions * * * * * * * * * * * * * * //
74
75  Foam::tmp<Foam::volScalarField>
76  Foam::mixtureViscosityModels::quadraticMixture::mu(const volScalarField&
    muc) const
77  {
```

```
    return
    (
        muc*(1.0 + 2.5*alpha_ + 5.2*sqr(alpha_))
    );
}


bool Foam::mixtureViscosityModels::quadraticMixture::read
(
    const dictionary& viscosityProperties
)
{
    return true;
}


// ************************************************************************* //
```

B.3 equilibriumParticle.H Relative Velocity Model

```
/*---------------------------------------------------------------------------*\
  =========                 |
  \\      /  F ield         | OpenFOAM: The Open Source CFD Toolbox
   \\    /   O peration     | Website:  https://openfoam.org
    \\  /    A nd           | Copyright (C) 2014-2019 OpenFOAM Foundation
     \\/     M anipulation  |
-------------------------------------------------------------------------------
License
    This file is part of OpenFOAM.

    OpenFOAM is free software: you can redistribute it and/or modify it
    under the terms of the GNU General Public License as published by
    the Free Software Foundation, either version 3 of the License, or
    (at your option) any later version.

    OpenFOAM is distributed in the hope that it will be useful, but
    WITHOUT
    ANY WARRANTY; without even the implied warranty of MERCHANTABILITY or
    FITNESS FOR A PARTICULAR PURPOSE.  See the GNU General Public License
    for more details.

    You should have received a copy of the GNU General Public License
    along with OpenFOAM.  If not, see <http://www.gnu.org/licenses/>.

```

```
Class
    Foam::relativeVelocityModels::equilibriumParticle

Description
    Equilibrium particle relative velocity model

SourceFiles
    equilibriumParticle.C

\*---------------------------------------------------------------------------*/

#ifndef equilibrium_particle_H
#define equilibrium_particle_H

#include "relativeVelocityModel.H"

// * * * * * * * * * * * * * * * * * * * * * * * * * * * * * * * * * * * * * //


namespace Foam
{
namespace relativeVelocityModels
{

/*---------------------------------------------------------------------------*\
                  Class equilibriumParticle Declaration
\*---------------------------------------------------------------------------*/

class equilibriumParticle
:
    public relativeVelocityModel
{
    // Private Data

  //- gravity
  scalar g_;

  //- particle diamter
  dimensionedScalar dp_;

  //- fluid dynamic viscosity
  dimensionedScalar muc_;

public:

```

```
    //- Runtime type information
    TypeName("equilibriumParticle");


    // Constructors

        //- Construct from components
        equilibriumParticle
        (
            const dictionary& dict,
            const incompressibleTwoPhaseInteractingMixture& mixture
        );


    //- Destructor
    ~equilibriumParticle();


    // Member Functions

        //- Update the diffusion velocity
        virtual void correct();
};


// * * * * * * * * * * * * * * * * * * * * * * * * * * * * * * * * * * * * //

} // End namespace relativeVelocityModels
} // End namespace Foam

// * * * * * * * * * * * * * * * * * * * * * * * * * * * * * * * * * * * * //

#endif
```

B.4 equilibriumParticle.C Relative Velocity Model

```
/*---------------------------------------------------------------------------*\
  =========                 |
  \\      /  F ield         | OpenFOAM: The Open Source CFD Toolbox
   \\    /   O peration     | Website:  https://openfoam.org
    \\  /    A nd           | Copyright (C) 2014-2018 OpenFOAM Foundation
     \\/     M anipulation  |
-------------------------------------------------------------------------------
License
```

```
9       This file is part of OpenFOAM.
10
11      OpenFOAM is free software: you can redistribute it and/or modify it
12      under the terms of the GNU General Public License as published by
13      the Free Software Foundation, either version 3 of the License, or
14      (at your option) any later version.
15
16      OpenFOAM is distributed in the hope that it will be useful, but
        WITHOUT
17      ANY WARRANTY; without even the implied warranty of MERCHANTABILITY or
18      FITNESS FOR A PARTICULAR PURPOSE.  See the GNU General Public License
19      for more details.
20
21      You should have received a copy of the GNU General Public License
22      along with OpenFOAM.  If not, see <http://www.gnu.org/licenses/>.
23
24  \*---------------------------------------------------------------------*/
25
26  #include "equilibriumParticle.H"
27  #include "addToRunTimeSelectionTable.H"
28
29  // * * * * * * * * * * * * * Static Data Members * * * * * * * * * * * //
30
31  namespace Foam
32  {
33  namespace relativeVelocityModels
34  {
35      defineTypeNameAndDebug(equilibriumParticle, 0);
36      addToRunTimeSelectionTable(relativeVelocityModel, equilibriumParticle
        , dictionary);
37  }
38  }
39
40
41  // * * * * * * * * * * * * * * Constructors  * * * * * * * * * * * * * //
42
43  Foam::relativeVelocityModels::equilibriumParticle::equilibriumParticle
44  (
45      const dictionary& dict,
46      const incompressibleTwoPhaseInteractingMixture& mixture
47  )
48  :
49      relativeVelocityModel(dict, mixture),
50
51      dp_("dp", dimLength, dict),
```

```
52
53      // Viscosity dimension had to be modified to achieve the velocity
        dimenions at the end
54      // The for loop does not account for units
55      muc_("muc", dimensionSet(1, -1, 0, 0, 0), dict),
56
57      g_(-9.81)
58
59
60  {
61  }
62
63
64  // * * * * * * * * * * * * * Destructor  * * * * * * * * * * * * * //
65
66  Foam::relativeVelocityModels::equilibriumParticle::~equilibriumParticle()
67  {}
68
69
70  // * * * * * * * * * * * * Member Functions  * * * * * * * * * * * * //
71
72  void Foam::relativeVelocityModels::equilibriumParticle::correct()
73  {
74
75      scalar positionSmall = 1e-8;
76
77
78      const volVectorField& U = mixture_.U();
79      const volVectorField& r = U.mesh().C();
80
81      auto f = rhoc_/rho()*(scalar(1.0) - alphad_)*dp_*dp_*(rhod_-rhoc_)/(
        scalar(18.)*muc_);
82
83      // compute the giant fraction in the expression for Udm
84      forAll(U.mesh().V(),celli)
85      {
86          Udm_[celli].component(0) = pow((r[celli].component(0)*U[celli].
        component(1)-r[celli].component(1)*U[celli].component(0))/(r[celli].
        component(0)*r[celli].component(0) + r[celli].component(1)*r[celli].
        component(1) + positionSmall), 2)*r[celli].component(0);
87
88          Udm_[celli].component(1) = pow((r[celli].component(0)*U[celli].
        component(1)-r[celli].component(1)*U[celli].component(0))/(r[celli].
        component(0)*r[celli].component(0) + r[celli].component(1)*r[celli].
        component(1) + positionSmall), 2)*r[celli].component(1);
```

```
89
90          Udm_[celli].component(2) = g_;
91
92      }
93      // multiply the terms that do not require U and r
94      Udm_ *= f;
95
96  }
97
98  // ************************************************************* //
```